

1 High-level cognition during story listening is reflected in
2 high-order dynamic correlations in neural activity patterns

3 Lucy L. W. Owen¹, Thomas H. Chang^{1,2}, and Jeremy R. Manning^{1,†}

¹Department of Psychological and Brain Sciences,
Dartmouth College, Hanover, NH

²Amazon.com, Seattle, WA

†Address correspondence to jeremy.r.manning@dartmouth.edu

4 August 11, 2021

5 **Abstract**

6 Our thoughts arise from coordinated patterns of interactions between brain structures that change with
7 our ongoing experiences. High-order dynamic correlations in neural activity patterns reflect different sub-
8 graphs of the brain's functional connectome that display homologous lower-level dynamic correlations. We
9 tested Here we test the hypothesis that high-level cognition is reflected in high-order dynamic correlations in
10 brain activity patterns. We developed develop an approach to estimating high-order dynamic correlations
11 in timeseries data, and we applied apply the approach to neuroimaging data collected as human
12 participants either listened listen to a ten-minute story or listened listen to a temporally scrambled version
13 of the story. We trained train across-participant pattern classifiers to decode (in held-out data) when in
14 the session each neural activity snapshot was collected. We found find that classifiers trained to decode
15 from high-order dynamic correlations yielded yield the best performance on data collected as participants
16 listened to the (unscrambled) story. By contrast, classifiers trained to decode data from scrambled versions
17 of the story yielded the best performance when they were trained using first-order dynamic correlations
18 or non-correlational activity patterns. We suggest that as our thoughts become more complex, they are
19 reflected in higher-order patterns of dynamic network interactions throughout the brain.

20 **Introduction**

21 A central goal in cognitive neuroscience is to elucidate the neural code: neural code: i.e., the mapping between
22 (a) mental states or cognitive representations and (b) neural activity patterns. One means of testing models of
23 the neural code is to ask how accurately that model is able to "translate" neural activity patterns into known
24 (or hypothesized) mental states or cognitive representations e.g.,^{1–9}. Training decoding models on different
25 types of neural features (Fig. 1a) can also help to elucidate which specific aspects of neural activity patterns
26 are informative about cognition and, by extension, which types of neural activity patterns might compose
27 the neural code. For example, prior work has used region of interest analyses to estimate the anatomical
28 locations of specific neural representations e.g.,¹⁰, or to compare the relative contributions to the neural
29 code of multivariate activity patterns versus dynamic correlations between neural activity patterns e.g.,^{11,12}.

30 An emerging theme in this literature is that cognition is mediated by dynamic interactions between brain
31 structures^{13–25}.

32 [Figure 1 about here.]

33 Studies of the neural code to date have primarily focused on univariate or multivariate neural patterns for
34 review see², or (more recently) on patterns of dynamic first-order correlations i.e., interactions between
35 pairs of brain structures;^{11,12,18,20–22}. What might the future of this line of work hold? For example,
36 is the neural code implemented through higher-order interactions between brain structures e.g., see²⁶?
37 Second-order correlations reflect *homologous* homologous patterns of correlation. In other words, if the
38 dynamic patterns of correlations between two regions, *A* and *B*, are similar to those between two other
39 regions, *C* and *D*, this would be reflected in the second-order correlations between (*A*–*B*) and (*C*–*D*). In
40 this way, second-order correlations identify similarities and differences between subgraphs of the brain’s
41 connectome. Analogously, third-order correlations reflect homologies between second-order correlations—
42 i.e., homologous patterns of homologous interactions between brain regions. More generally, higher-order
43 correlations reflect homologies between patterns of lower-order correlations. We can then ask: which
44 “orders” of interaction are most reflective of high-level cognitive processes?

45 One reason one might expect to see homologous networks in a dataset is related to the notion that network
46 dynamics reflect ongoing neural computations or cognitive processing e.g.,²⁷. If the nodes in two brain
47 networks are interacting (within each network) in similar ways then, according to our characterization
48 of network dynamics, we refer to the similarities between those patterns of interaction as higher-order
49 correlations. When higher-order correlations are themselves changing over time, we can also attempt to
50 capture and characterize those high-order dynamics.

51 Another central question pertains to the extent to which the neural code is carried by activity patterns that
52 directly reflect ongoing cognition e.g., following^{1,2}, versus the dynamic properties of the network structure
53 itself, independent of specific activity patterns in any given set of regions e.g., following¹⁶. For example,
54 graph measures such as centrality and degree²⁸ may be used to estimate how a given brain structure is
55 “communicating” with other structures, independently of the specific neural representations carried by
56 those structures. If one considers a brain region’s position in the network (e.g., its eigenvector centrality) as
57 a dynamic property, one can compare how the positions of different regions are correlated, and/or how those
58 patterns of correlations change over time. We can also compute higher-order patterns in these correlations
59 to characterize homologous subgraphs in the connectome that display similar changes in their constituent
60 brain structures’ interactions with the rest of the brain.

61 To gain insights into the above aspects of the neural code, we developed a computational framework

62 for estimating dynamic high-order correlations in timeseries data. This framework provides an important
63 advance, in that it enables us to examine patterns of higher-order correlations that are computationally
64 intractable to estimate via conventional methods. Given a multivariate timeseries, our framework pro-
65 vides timepoint-by-timepoint estimates of the first-order correlations, second-order correlations, and so
66 on. Our approach combines a kernel-based method for computing dynamic correlations in timeseries
67 data with a dimensionality reduction step (Fig. 1b) that projects the resulting dynamic correlations into
68 a low-dimensional space. We explored two dimensionality reduction approaches: principle components
69 analysis PCA,²⁹, which preserves an approximately invertible transformation back to the original data e.g.,
70 this follows related approaches taken by³⁰⁻³²; and a second non-invertible algorithm for computing dynamic
71 patterns in eigenvector centrality³³. This latter approach characterizes correlations between each feature
72 dimension's relative *position position* in the network (at each moment in time) in favor of the specific activity
73 histories of different features also see^{26,34,35}.

74 We validated our approach using synthetic data where the underlying correlations were known. We
75 then applied our framework to a neuroimaging dataset collected as participants listened to either an audio
76 recording of a ten-minute story, listened to a temporally scrambled version of the story, or underwent a
77 resting state scan³⁶. Temporal scrambling has been used in a growing number of studies, largely by Uri
78 Hasson's group, to identify brain regions that are sensitive to higher-order and longer-timescale information
79 (e.g., cross-sensory integration, rich narrative meaning, complex situations, etc.) versus regions that are
80 primarily sensitive to low-order (e.g., sensory) information. For example,³⁷ argues that when brain areas
81 are sensitive to fine versus coarse temporal scrambling, this indicates that they are "higher order" in the
82 sense that they process contextual information pertaining to further-away timepoints. By contrast, low-level
83 regions, such as primary sensory cortices, do not meaningfully change their responses (after correcting for
84 presentation order) even when the stimulus is scrambled at fine timescales.

85 We used a subset of the story listening and rest data to train across-participant classifiers to decode
86 listening times (of groups of participants) using a blend of neural features (comprising neural activity
87 patterns, as well as different orders of dynamic correlations between those patterns that were inferred
88 using our computational framework). We found that both the PCA-based and eigenvector centrality-based
89 approaches yielded neural patterns that could be used to decode accurately (i.e., well above chance). Both
90 approaches also yielded the best decoding accuracy for data collected during (intact) story listening when
91 high-order (PCA: second-order; eigenvector centrality: fourth-order) dynamic correlation patterns were
92 included as features. When we trained classifiers on the scrambled stories or resting state data, only
93 (relatively) lower-order dynamic patterns were informative to the decoders. Taken together, our results
94 indicate that high-level cognition is supported by high-order dynamic patterns of communication between

95 brain structures.

96 Results

97 We sought to understand whether high-level cognition is reflected in dynamic patterns of high-order cor-
98 relations. To that end, we developed a computational framework for estimating the dynamics of stimulus-
99 driven high-order correlations in multivariate timeseries data (see *Dynamic inter-subject functional connectivity*
100 (*DISFC*) and *Dynamic higher-order correlations**Dynamic inter-subject functional connectivity (DISFC)* and
101 *Dynamic higher-order correlations*). We evaluated the efficacy of this framework at recovering known pat-
102 terns in several synthetic datasets (see *Synthetic data: simulating dynamic first-order correlations* and *Synthetic*
103 *data: simulating dynamic higher-order correlations**Synthetic data: simulating dynamic first-order correlations*
104 *and Synthetic data: simulating dynamic higher-order correlations*). We then applied the framework to a
105 public fMRI dataset collected as participants listened to an auditorily presented story, listened to a tem-
106 porally scrambled version of the story, or underwent a resting state scan (see *Functional neuroimaging data*
107 *collected during story listening**Functional neuroimaging data collected during story listening*). We used the
108 relative decoding accuracies of classifiers trained on different sets of neural features to estimate which types
109 of features reflected ongoing cognitive processing.

110 Recovering known dynamic *first-order* correlations*from synthetic data*

111 *Recovering dynamic first-order correlations*

112 We generated synthetic datasets that differed in how the underlying first-order correlations changed over
113 time. For each dataset, we applied Equation 4 with a variety of kernel shapes and widths. We assessed how
114 well the true underlying correlations at each timepoint matched the recovered correlations (Fig. 2). For every
115 kernel and dataset we tested, our approach recovered the correlation dynamics we embedded into the data.
116 However, the quality of these recoveries varied across different synthetic datasets in a kernel-dependent
117 way.

118 [Figure 2 about here.]

119 In general, wide monotonic kernel shapes (Laplace, Gaussian), and wider kernels (within a shape),
120 performed best when the correlations varied gradually from moment-to-moment (Figs. 2a, c, and d). In the
121 extreme, as the rate of change in correlations approaches 0 (Fig. 2a), an infinitely wide kernel would exactly
122 recover the Pearson's correlation (e.g., compare Eqns. 1 and 4).

123 When the correlation dynamics were unstructured in time (Fig. 2b), a Dirac δ kernel (infinitely narrow) performed best. This is because, when every timepoint's correlations are independent ~~from~~of the correlations at every other timepoint, averaging data over time dilutes the available signal. Following a similar pattern, holding kernel shape fixed, narrower kernel parameters better recovered randomly varying correlations.

128 **Recovering dynamic higher-order correlations**

129 **Recovering known dynamic higher-order correlations**

130 Following our approach to evaluating our ability to recover known dynamic first-order correlations from
131 synthetic data, we generated an analogous second set of synthetic datasets that we designed to exhibit known
132 dynamic first-order ~~and~~ and second-order correlations (see *Synthetic data: simulating dynamic higher-order*
133 ~~correlations~~Synthetic data: simulating dynamic higher-order correlations). We generated a total of 400
134 datasets (100 datasets for each category) that varied in how the first-order and second-order correlations
135 changed over time. We then repeatedly applied Equation 4 using the overall best-performing kernel from
136 our first-order tests (a Laplace kernel with a width of 20; Fig. 2) to assess how closely the recovered dynamic
137 correlations matched the dynamic correlations we had embedded into the datasets.

138 Overall, we found that we could reliably recover both first-order and second-order correlations from
139 the synthetic data (Fig. 3). When the correlations were stable for longer intervals, or changed gradually
140 (constant, ramping, and event datasets), recovery performance was relatively high, and we were better
141 able to recover dynamic first-order correlations than second-order correlations. This is because errors in
142 our ~~estimation~~ estimation procedure at lower orders necessarily propagate to higher orders (since lower-
143 order correlations are used to estimate higher-order correlations). Conversely, when the correlations were
144 particularly ~~unstable~~ unstable (random datasets), we better recovered second-order correlations. This is
145 because noise in our ~~data generation~~ data generation procedure propagates from higher orders to lower
146 orders (see *Synthetic data: simulating dynamic high-order correlations*Synthetic data: simulating dynamic
147 high-order correlations).

148 [Figure 3 about here.]

149 We also examined the impact of the data duration (Fig. S3) and complexity (number of zero-order features;
150 Fig. S4) on our ability to accurately recover ground truth first-order and second-order dynamic correlations.
151 In general, we found that our approach better recovers ground truth dynamic correlations from longer
152 duration timeseries data. We also found that our approach tends to best recover data generated using fewer

153 zero-order features (i.e., lower complexity), although this tendency was not strictly monotonic. Further,
154 because our data generation procedure requires $O(K^4)$ memory to generate a second-order timeseries with K
155 zero-order features, we were not able to fully explore how the number of zero-order features affects recovery
156 accuracy as the number of features gets larger (e.g., as it approaches the number of features present in the
157 fMRI data we examine below). Although we were not able to formally test this to our satisfaction, we expect
158 that accurately estimating dynamic high-order correlations would require data with many more zero-order
159 features than we were able to simulate. Our reasoning is that high-order correlations necessarily involve
160 larger numbers of lower-order features, so achieving adequate “resolution” high-order timeseries might
161 require many low-order features.

162 Taken together, our explorations using synthetic data indicated that we are able to partially, but not
163 perfectly, recover ground truth dynamic first-order and second-order correlations. This suggests that our
164 modeling approach provides a meaningful (if noisy) estimate of high-order correlations. We next turned
165 to analyses of human fMRI data to examine whether the recovered dynamics might reflect the dynamics of
166 human cognition during a naturalistic story-listening task.

167 Cognitively relevant dynamic high-order correlations in fMRI data

168 We used across-participant temporal decoders to identify cognitively relevant neural patterns in fMRI
169 data (see *Forward inference and decoding accuracy*[Forward inference and decoding accuracy](#)). The dataset
170 we examined collected by³⁶ comprised four experimental conditions that exposed participants to stimuli
171 that varied systematically in how cognitively engaging they were. The *intact experimental condition*
172 [intact experimental condition \(intact\)](#) had participants listen to an audio recording of a 10-minute story. The
173 *paragraph-scrambled experimental condition*[paragraph-scrambled experimental condition \(paragraph\)](#) had
174 participants listen to a temporally scrambled version of the story, where the paragraphs occurred out of order
175 (but where the same total set of paragraphs were presented over the full listening interval). All participants
176 in this condition experienced the scrambled paragraphs in the same order. The *word-scrambled experimental*
177 [condition word-scrambled experimental condition \(word\)](#) had participants listen to a temporally scrambled
178 version of the story where the words in the story occurred in a random order. All participants in the word
179 condition experienced the scrambled words in the same order. Finally, in a *rest experimental condition*
180 [rest experimental condition \(rest\)](#), participants lay in the scanner with no overt stimulus, with their eyes
181 open (blinking as needed). This public dataset provided a convenient means of testing our hypothesis that
182 different levels of cognitive processing and engagement are reflected in different orders of brain activity
183 dynamics.

184

[Figure 4 about here.]

185 In brief, we computed timeseries of dynamic high-order correlations that were similar across participants
 186 in each of two randomly assigned groups: a training group and a test group. We then trained classifiers
 187 on the training group's data to match each sample from the test group with a stimulus timepoint. Each
 188 classifier comprised a weighted blend of neural patterns that reflected up to n^{th} -order dynamic correlations
 189 (see *Feature weighting and testing*, Fig. 10*Feature weighting and testing*). We repeated this process for
 190 $n \in \{0, 1, 2, \dots, 10\}$. Our examinations of synthetic data suggested that none of the kernels we examined
 191 were "universal" in the sense of optimally recovering underlying correlations regardless of the temporal
 192 structure of those correlations. We found a similar pattern in the (real) fMRI data, whereby different kernels
 193 yielded different decoding accuracies, but no single kernel emerged as the clear "best." In our analyses
 194 of neural data, we therefore averaged our decoding results over a variety of kernel shapes and widths
 195 in order to identify results that were robust to specific kernel parameters (see *Identifying robust decoding*
 196 *results**Identifying robust decoding results*).

197 Our approach to estimating dynamic high-order correlations entails mapping the high-dimensional
 198 feature space of correlations (represented by a T by $O(K^2)$ matrix) onto a lower-dimensional feature space
 199 (represented by a T by K matrix). We carried out two sets of analyses that differed in how this mapping was
 200 computed. The first set of analyses used PCA to find a low-dimensional embedding of the original dynamic
 201 correlation matrices (Fig. 4a,b). The second set of analyses characterized correlations in dynamics of each
 202 feature's eigenvector centrality, but did not preserve the underlying activity dynamics (Fig. 4c,d).

203

[Figure 5 about here.]

204 Both sets of temporal decoding analyses yielded qualitatively similar results for the auditory (non-rest)
 205 conditions of the experiment (Fig. 4: pink, green, and teal lines; Fig. 5: three leftmost columns). The highest
 206 decoding accuracy for participants who listened to the intact (unscrambled) story was achieved using high-
 207 order dynamic correlations (PCA: second-order; eigenvector-centrality: fourth-order). Scrambled versions
 208 of the story were best decoded by lower-order correlations (PCA/paragraph: first-order; PCA/word: order
 209 zero; eigenvector centrality/paragraph: order zero; eigenvector centrality/word: order zero). The two sets
 210 of analyses yielded different decoding results on resting state data (Fig. 4: purple lines; Fig. 5: rightmost
 211 column). We note that, while the resting state times could be decoded reliably, the accuracies were only very
 212 slightly above chance. We speculate that the decoders might have picked up on attentional drift, boredom,
 213 or tiredness; we hypothesize that these all increased throughout the resting state scan. The decoders might
 214 be picking up on aspects of these loosely defined cognitive states that are common across individuals. The

215 PCA-based approach achieved the highest resting state decoding accuracy using order zero features (non-
216 correlational, activation-based), whereas the eigenvector centrality-based approach achieved the highest
217 resting state decoding accuracy using second-order correlations. Taken together, these analyses indicate
218 that high-level cognitive processing (while listening to the intact story) is reflected in the dynamics of high-
219 order correlations in brain activity, whereas lower-level cognitive processing (while listening to scrambled
220 versions of the story that lack rich meaning) is reflected in the dynamics of lower-order correlations and
221 non-correlational activity dynamics. Further, these patterns are associated both with the underlying activity
222 patterns (characterized using PCA) and also with the changing relative positions that different brain areas
223 occupy in their associated networks (characterized using eigenvector centrality).

224 [Figure 6 about here.]

225 Having established that patterns of high-order correlations are informative to decoders, we next won-
226 dered which specific networks of brain regions contributed most to these patterns. As a representative
227 example, we selected the kernel parameters that yielded decoding accuracies that were the most strongly
228 correlated (across conditions and orders) with the average accuracies across all of the kernel parameters we
229 examined. Using Figure 4c as a template, the best-matching kernel was a Laplace kernel with a width of 50
230 (Fig. 9d; also see Fig. S9). We used this kernel to compute a single K by K n^{th} -order DISFC matrix for each
231 experimental condition. We then used Neurosynth³⁸ to compute the terms most highly associated with
232 the most strongly correlated pairs of regions in each of these matrices (Fig. 6; see *Reverse inference*Reverse
233 inference).

234 For all of the story listening conditions (intact, paragraph, and word; top three rows of Fig. 6), we
235 found that first- and second-order correlations were most strongly associated with auditory and speech
236 processing areas. During intact story listening, third-order correlations reflected integration with visual
237 areas, and fourth-order correlations reflected integration with areas associated with high-level cognition
238 and cognitive control, such as the ventrolateral prefrontal cortex. However, when participants listened to
239 temporally scrambled stories, these higher-order correlations instead involved interactions with additional
240 regions associated with speech and semantic processing (second and third rows of Fig. 6). By contrast, we
241 found a much different set of patterns in the resting state data (Fig. 6, bottom row). First-order resting state
242 correlations were most strongly associated with regions involved in counting and numerical understand-
243 ing. Second-order resting state correlations were strongest in visual areas; third-order correlations were
244 strongest in task-positive areas; and fourth-order correlations were strongest in regions associated with
245 autobiographical and episodic memory. We carried out analogous analyses to create maps (and decode
246 the top associated Neurosynth terms) for up to fifteenth-order correlations (Figs. S5, S6, S7, and S8). Of

247 note, examining fifteenth-order correlations between 700 nodes using conventional methods would have
248 required storing roughly $\frac{700^{2 \times 15}}{2} \approx 1.13 \times 10^{85}$ floating point numbers—assuming single-precision (32 bits
249 each), this would require roughly 32 times as many bits as there are molecules in the known universe!
250 Although these fifteenth-order correlations do appear (visually) to have some well-formed structure, we
251 provide this latter example primarily as a demonstration of the efficiency and scalability of our approach.

252 Discussion

253 We tested the hypothesis that high-level cognition is reflected in high-order brain network dynamics e.g.,
254 see^{19,26}. We examined high-order network dynamics in functional neuroimaging data collected during a
255 story listening experiment. When participants listened to an auditory recording of the story, participants
256 exhibited similar high-order brain network dynamics. By contrast, when participants instead listened to
257 temporally scrambled recordings of the story, only lower-order brain network dynamics were similar across
258 participants. Our results indicate that higher orders of network interactions support higher-level aspects of
259 cognitive processing (Fig. 7).

260 [Figure 7 about here.]

261 The notion that cognition is reflected in (and possibly mediated by) patterns of first-order network dy-
262 namics has been suggested by or proposed in myriad empirical studies and reviews e.g.,^{11,12,17,18,20–22,24,25,32,39–42}.
263 Our study extends this line of work by finding cognitively relevant *higher-order* *higher-order* network dy-
264 namics that reflect ongoing cognition. Our findings also complement other work that uses graph theory
265 and topology to characterize how brain networks reconfigure during cognition e.g.,^{16,26,30,31,34,35,43}.

266 An open question not addressed by our study pertains to how different structures integrate incoming
267 information with different time constants. For example, one line of work suggests that the cortical surface
268 comprises a structured map such that nearby brain structures process incoming information at similar
269 timescales. Low-level sensory areas integrate information relatively quickly, whereas higher-level regions
270 integrate information relatively slowly^{37,44–49}. A similar hierarchy appears to play a role in predicting future
271 events⁵⁰. Other related work in human and mouse brains indicates that the temporal response profile of a
272 given brain structure may relate to how strongly connected that structure is with other brain areas⁵¹. Further
273 study is needed to understand the role of temporal integration at different scales of network interaction,
274 and across different anatomical structures. Importantly, our analyses do not speak to the physiological
275 basis of higher-order dynamics, and could reflect nonlinearities, chaotic patterns, non-stationarities, and/or
276 multistability, etc. However, our decoding analyses do indicate that higher-order dynamics are consistent

277 across individuals, and therefore unlikely to reflect non-stimulus-driven dynamics that are unlikely to be
278 similar across individuals.

279 One limitation of our approach relates to how noise propagates in our estimation procedure. Specifi-
280 cally, our procedure for estimating high-order dynamic correlations depends on estimates of lower-order
281 dynamic correlations. This means that our measures of which higher-order patterns are reliable and stable
282 across experimental conditions are partially confounded with the stability of lower-order patterns. Prior
283 work suggests that the stability of what we refer to here as first-order dynamics likely varies across the
284 experimental conditions we examined³⁶. Therefore a caveat to our claim that richer stimuli evoke more
285 stable higher-order dynamics is that our approach assumes that those high-order dynamics reflect relations
286 or interactions between lower-order features.

287 Another potential limitation of our approach relates to recent work suggesting that the brain undergoes
288 rapid state changes, for example across event boundaries e.g.,^{44, 52} used hidden semi-Markov models to es-
289 timate state-specific network dynamics also see⁵³. Our general approach might be extended by considering
290 putative state transitions. For example, rather than weighting all timepoints using a similar kernel (Eqn. 4),
291 the kernel function could adapt on a timepoint-by-timepoint basis such that only timepoints determined to
292 be in the same “state” were given non-zero weight.

293 Identifying high-order network dynamics associated with high-level cognition required several impor-
294 tant methods advances. First, we used kernel-based dynamic correlations to extended the notion of (static)
295 inter-subject functional connectivity³⁶ to a dynamic measure of inter-subject functional connectivity (DISFC)
296 that does not rely on sliding windows e.g., as in¹¹, and that may be computed at individual timepoints. This
297 allowed us to precisely characterize stimulus-evoked network dynamics that were similar across individ-
298 uals. Second, we developed a computational framework for efficiently and scalably estimating high-order
299 dynamic correlations. Our approach uses dimensionality reduction algorithms and graph measures to
300 obtain low-dimensional embeddings of patterns of network dynamics. Third, we developed an analysis
301 framework for identifying robust decoding results by carrying out our analyses using a range of parameter
302 values and identifying which results were robust to specific parameter choices. By showing that high-level
303 cognition is reflected in high-order network dynamics, we have elucidated the next step on the path towards
304 understanding the neural basis of cognition.

305 **Methods**

306 Our general approach to efficiently estimating high-order dynamic correlations comprises four general
307 steps (Fig. 8). First, we derive a kernel-based approach to computing dynamic pairwise correlations in

308 a T (timepoints) by K (features) multivariate timeseries, \mathbf{X}_0 . This yields a T by $O(K^2)$ matrix of dynamic
 309 correlations, \mathbf{Y}_1 , where each row comprises the upper triangle and diagonal of the correlation matrix at
 310 a single timepoint, reshaped into a row vector (this reshaped vector is $(\frac{K^2-K}{2} + K)$ -dimensional). Second,
 311 we apply a dimensionality reduction step to project the matrix of dynamic correlations back onto a K -
 312 dimensional space. This yields a T by K matrix, \mathbf{X}_1 , that reflects an approximation of the dynamic correlations
 313 reflected in the original data. Third, we use repeated applications of the kernel-based dynamic correlation
 314 step to \mathbf{X}_n and the dimensionality reduction step to the resulting \mathbf{Y}_{n+1} to estimate high-order dynamic
 315 correlations. Each application of these steps to a T by K time series \mathbf{X}_n yields a T by K matrix, \mathbf{X}_{n+1} , that
 316 reflects the dynamic correlations between the columns of \mathbf{X}_n . In this way, we refer to n as the *order* order of the
 317 timeseries, where \mathbf{X}_0 (order 0) denotes the original data and \mathbf{X}_n denotes (approximated) n^{th} -order dynamic
 318 correlations between the columns of \mathbf{X}_0 . Finally, we use a cross-validation-based decoding approach to
 319 evaluate how well information contained in a given order (or weighted mixture of orders) may be used
 320 to decode relevant cognitive states. If including a given \mathbf{X}_n in the feature set yields higher classification
 321 accuracy on held-out data, we interpret this as evidence that the given cognitive states are reflected in
 322 patterns of n^{th} -order correlations.

323 All of the code used to produce the figures and results in this manuscript, along with links to the
 324 corresponding datasets, may be found at github.com/ContextLab/timecorr-paper. In addition, we have
 325 released a Python toolbox for computing dynamic high-order correlations in timeseries data; our toolbox
 326 may be found at timecorr.readthedocs.io.

327 [Figure 8 about here.]

328 Kernel-based approach for computing dynamic correlations

Given a T by K matrix of observations, \mathbf{X} , we can compute the (static) Pearson's correlation between any
 pair of columns, $\mathbf{X}(\cdot, i)$ and $\mathbf{X}(\cdot, j)$ using²⁹:

$$\text{corr}(\mathbf{X}(\cdot, i), \mathbf{X}(\cdot, j)) = \frac{\sum_{t=1}^T (\mathbf{X}(t, i) - \bar{\mathbf{X}}(\cdot, i))(\mathbf{X}(t, j) - \bar{\mathbf{X}}(\cdot, j))}{\sqrt{\sum_{t=1}^T \sigma_{\mathbf{X}(\cdot, i)}^2 \sigma_{\mathbf{X}(\cdot, j)}^2}}, \text{ where} \quad (1)$$

$$\bar{\mathbf{X}}(\cdot, k) = \frac{1}{T} \sum_{t=1}^T \mathbf{X}(t, k), \text{ and} \quad (2)$$

$$\sigma_{\mathbf{X}(\cdot, k)}^2 = \frac{1}{T} \sum_{t=1}^T (\mathbf{X}(t, k) - \bar{\mathbf{X}}(\cdot, k))^2 \quad (3)$$

329 We can generalize this formula to compute time-varying correlations by incorporating a *kernel function*
 330 *kernel function* that takes a time t as input, and returns how much the observed data at each timepoint
 331 $\tau \in [-\infty, \infty]$ contributes to the estimated instantaneous correlation at time t Fig. 9; also see⁵⁴ for a similar
 332 approach.

333 [Figure 9 about here.]

Given a kernel function $\kappa_t(\cdot)$ for timepoint t , evaluated at timepoints $\tau \in [1, \dots, T]$, we can update the static correlation formula in Equation 1 to estimate the *instantaneous correlation* *instantaneous correlation* at timepoint t :

$$\text{timecorr}_{\kappa_t}(\mathbf{X}(\cdot, i), \mathbf{X}(\cdot, j)) = \frac{\sum_{\tau=1}^T (\mathbf{X}(\tau, i) - \tilde{\mathbf{X}}_{\kappa_t}(\cdot, i))(\mathbf{X}(\tau, j) - \tilde{\mathbf{X}}_{\kappa_t}(\cdot, j))}{\sqrt{\sum_{\tau=1}^T \tilde{\sigma}_{\kappa_t}^2(\mathbf{X}(\cdot, i)) \tilde{\sigma}_{\kappa_t}^2(\mathbf{X}(\cdot, j))}}, \text{ where} \quad (4)$$

$$\tilde{\mathbf{X}}_{\kappa_t}(\cdot, k) = \sum_{\tau=1}^T \kappa_t(\tau) \mathbf{X}(\tau, k), \quad (5)$$

$$\tilde{\sigma}_{\kappa_t}^2(\mathbf{X}(\cdot, k)) = \sum_{\tau=1}^T (\mathbf{X}(\tau, k) - \tilde{\mathbf{X}}_{\kappa_t}(\cdot, k))^2. \quad (6)$$

334 Here $\text{timecorr}_{\kappa_t}(\mathbf{X}(\cdot, i), \mathbf{X}(\cdot, j))$ reflects the correlation at time t between columns i and j of \mathbf{X} , estimated using
 335 the kernel κ_t . We evaluate Equation 4 in turn for each pair of columns in \mathbf{X} and for kernels centered on each
 336 timepoint in the timeseries, respectively, to obtain a T by K by K timeseries of dynamic correlations, \mathbf{Y} . For
 337 convenience, we then reshape the upper triangles and diagonals of each timepoint's symmetric correlation
 338 matrix into a row vector to obtain an equivalent T by $(\frac{K^2-K}{2} + K)$ matrix.

339 Dynamic inter-subject functional connectivity (DISFC)

Equation 4 provides a means of taking a single observation matrix, \mathbf{X}_n and estimating the dynamic correlations from moment to moment, \mathbf{Y}_{n+1} . Suppose that one has access to a set of multiple observation matrices that reflect the same phenomenon. For example, one might collect neuroimaging data from several experimental participants, as each participant performs the same task (or sequence of tasks). Let $\mathbf{X}_n^1, \mathbf{X}_n^2, \dots, \mathbf{X}_n^P$ reflect the T by K observation matrices ($n = 0$) or reduced correlation matrices ($n > 0$) for each of P participants in an experiment. We can use *inter-subject functional connectivity* *inter-subject functional connectivity* ISFC;^{36,55} to compute the stimulus-driven correlations reflected in the multi-participant dataset

at a given timepoint t using:

$$\bar{\mathbf{C}}(t) = M \left(R \left(\frac{1}{2P} \sum_{p=1}^P Z(\mathbf{Y}_{n+1}^p(t))^\top + Z(\mathbf{Y}_{n+1}^p(t)) \right) \right), \quad (7)$$

where M extracts and vectorizes the upper triangle and diagonal of a symmetric matrix, Z is the Fisher z-transformation⁵⁶:

$$Z(r) = \frac{\log(1+r) - \log(1-r)}{2}, \quad (8)$$

R is the inverse of Z :

$$R(z) = \frac{\exp(2z-1)}{\exp(2z+1)}, \quad (9)$$

and $\mathbf{Y}_{n+1}^p(t)$ denotes the correlation matrix at timepoint t (Eqn. 4) between each column of \mathbf{X}_n^p and each column of the average \mathbf{X}_n from all ~~other~~ other participants, $\bar{\mathbf{X}}_n^p$:

$$\bar{\mathbf{X}}_n^p = \frac{1}{P-1} \sum_{q \in \setminus p} \mathbf{X}_n^q, \quad (10)$$

340 where $\setminus p$ denotes the set of all participants other than participant p . In this way, the T by $(\frac{K^2-K}{2} + K)$ DISFC
341 matrix $\bar{\mathbf{C}}$ provides a time-varying extension of the ISFC approach developed by³⁶.

342 Low-dimensional representations of dynamic correlations

343 Given a T by $(\frac{K^2-K}{2} + K)$ matrix of n^{th} -order dynamic correlations, \mathbf{Y}_n , we propose two general approaches
344 to computing a T by K low-dimensional representation of those correlations, \mathbf{X}_n . The first approach uses
345 dimensionality reduction algorithms to project \mathbf{Y}_n onto a K -dimensional space. The second approach uses
346 graph measures to characterize the relative positions of each feature ($k \in [1, \dots, K]$) in the network defined
347 by the correlation matrix at each timepoint.

348 Dimensionality reduction-based approaches to computing \mathbf{X}_n

349 The modern toolkit of dimensionality reduction algorithms include Principal Components Analysis PCA;²⁹,
350 Probabilistic PCA PPCA;⁵⁷, Exploratory Factor Analysis EFA;⁵⁸, Independent Components Analysis ICA;^{59,60},
351 t-Stochastic Neighbor Embedding t-SNE;⁶¹, Uniform Manifold Approximation and Projection UMAP;⁶²,
352 non-negative matrix factorization NMF;⁶³, Topographic Factor Analysis TFA;⁶⁴, Hierarchical Topographic

353 Factor analysis HTFA;¹¹, Topographic Latent Source Analysis TLSA;⁶⁵, dictionary learning^{66,67}, and deep
354 auto-encoders⁶⁸, among others. While complete characterizations of each of these algorithms is beyond the
355 scope of the present manuscript, the general intuition driving these approaches is to compute the T by K
356 matrix, \mathbf{X} , that is closest to the original T by J matrix, \mathbf{Y} , where (typically) $K \ll J$. The different approaches
357 place different constraints on what properties \mathbf{X} must satisfy and which aspects of the data are compared
358 (and how) in order to optimize how well \mathbf{X} approximates \mathbf{Y} .

359 Applying dimensionality reduction algorithms to \mathbf{Y} yields an \mathbf{X} whose columns reflect weighted combi-
360 nations (or nonlinear transformations) of the original columns of \mathbf{Y} . This has two main consequences. First,
361 with each repeated dimensionality reduction, the resulting \mathbf{X}_n has lower and lower fidelity (with respect to
362 what the “true” \mathbf{Y}_n might have looked like without using dimensionality reduction to maintain tractability).
363 In other words, computing \mathbf{X}_n is a lossy operation. Second, whereas each column of \mathbf{Y}_n may be mapped
364 directly onto specific pairs of columns of \mathbf{X}_{n-1} , the columns of \mathbf{X}_n reflect weighted combinations and/or
365 nonlinear transformations of the columns of \mathbf{Y}_n . Many dimensionality reduction algorithms are invertible
366 (or approximately invertible). However, attempting to map a given \mathbf{X}_n back onto the original feature space
367 of \mathbf{X}_0 will usually require $O(TK^2)$ space and therefore becomes intractable as n or K grow large.

368 **Graph measure approaches to computing \mathbf{X}_n**

369 The above dimensionality reduction approaches to approximating a given \mathbf{Y}_n with a lower-dimensional
370 \mathbf{X}_n preserve a (potentially recombined and transformed) mapping back to the original data in \mathbf{X}_0 . We also
371 explore graph measures that instead characterize each feature’s relative *position* in the broader
372 network of interactions and connections. To illustrate the distinction between the two general approaches
373 we explore, suppose a network comprises nodes A and B , along with several other nodes. If A and B exhibit
374 uncorrelated activity patterns, then by definition the functional connection (correlation) between them will
375 be close to 0. However, if A and B each interact with *other* nodes in similar ways, we might attempt
376 to capture those similarities between A ’s and B ’s interactions with those other members of the network.

377 In general, graph measures take as input a matrix of interactions (e.g., using the above notation, a K
378 by K correlation matrix or binarized correlation matrix reconstituted from a single timepoint’s row of \mathbf{Y}),
379 and return as output a set of K measures describing how each node (feature) sits within that correlation
380 matrix with respect to the rest of the population. Widely used measures include betweenness centrality the
381 proportion of shortest paths between each pair of nodes in the population that involves the given node in
382 question; e.g.,^{69–73}; diversity and dissimilarity characterizations of how differently connected a given node
383 is from others in the population; e.g.,^{74–76}; eigenvector centrality and pagerank centrality measures of how

384 influential a given node is within the broader network; e.g.,⁷⁷⁻⁸⁰; transfer entropy and flow coefficients a
385 measure of how much information is flowing from a given node to other nodes in the network; e.g.,^{81,82};
386 k -coreness centrality a measure of the connectivity of a node within its local subgraph; e.g.,^{83,84}; within-
387 module degree a measure of how many connections a node has to its close neighbors in the network;
388 e.g.,⁸⁵; participation coefficient a measure of the diversity of a node's connections to different subgraphs
389 in the network; e.g.,⁸⁵; and subgraph centrality a measure of a node's participation in all of the network's
390 subgraphs; e.g.,⁸⁶; among others.

391 For a given graph measure, $\eta : \mathbb{R}^{K \times K} \rightarrow \mathbb{R}^K$, we can use η to transform each row of \mathbf{Y}_n in a way that
392 characterizes the corresponding graph properties of each column. This results in a new T by K matrix,
393 \mathbf{X}_n , that reflects how the features reflected in the columns of \mathbf{X}_{n-1} participate in the network during each
394 timepoint (row).

395 Dynamic higher-order correlations

396 Because \mathbf{X}_n has the same shape as the original data \mathbf{X}_0 , approximating \mathbf{Y}_n with a lower-dimensional \mathbf{X}_n
397 enables us to estimate high-order dynamic correlations in a scalable way. Given a T by K input matrix, the
398 output of Equation 4 requires $O(TK^2)$ space to store. Repeated applications of Equation 4 (i.e., computing
399 dynamic correlations between the columns of the outputted dynamic correlation matrix) each require
400 exponentially more space; in general the n^{th} -order dynamic correlations of a T by K timeseries occupies
401 $O(TK^{2^n})$ space. However, when we approximate or summarize the output of Equation 4 with a T by K matrix
402 (as described above), it becomes feasible to compute even very high-order correlations in high-dimensional
403 data. Specifically, approximating the n^{th} -order dynamic correlations of a T by K timeseries requires only
404 $O(TK^2)$ additional space— the same as would be required to compute first-order dynamic correlations. In
405 other words, the space required to store $n + 1$ multivariate timeseries reflecting up to n^{th} order correlations
406 in the original data scales linearly with n using our approach (Fig. 8).

407 Data

408 We examined two types of data: synthetic data and human functional neuroimaging data. We constructed
409 and leveraged the synthetic data to evaluate our general approach for a related validation approach see⁸⁷.
410 Specifically, we tested how well Equation 4 could be used to recover known dynamic correlations using
411 different choices of kernel (κ ; Fig. 9), for each of several synthetic datasets that exhibited different temporal
412 properties. We also simulated higher-order correlations and tested how well Equation 4 could recover these
413 correlations using the best kernel from the previous synthetic data analyses. We then applied our approach

414 to a functional neuroimaging dataset to test the hypothesis that ongoing cognitive processing is reflected
415 in high-order dynamic correlations. We used an across-participant classification test to estimate whether
416 dynamic correlations of different orders contain information about which timepoint in a story participants
417 were listening to.

418 **Synthetic data: simulating dynamic first-order correlations**

419 We constructed a total of 400 different multivariate timeseries, collectively reflecting a total of 4 qualitatively
420 different patterns of dynamic first-order correlations (i.e., 100 datasets reflecting each type of dynamic pat-
421 tern). Each timeseries comprised 50 features (dimensions) that varied over 300 timepoints. The observations
422 at each timepoint were drawn from a zero-mean multivariate Gaussian distribution with a covariance matrix
423 defined for each timepoint as described below. We drew the observations at each timepoint independently
424 from the draws at all other timepoints; in other words, for each observation $s_t \sim \mathcal{N}(\mathbf{0}, \Sigma_t)$ at timepoint t ,
425 $p(s_t) = p(s_t | s_{\setminus t})$.

Constant. We generated data with stable underlying correlations to evaluate how Equation 4 characterized correlation “dynamics” when the ground truth correlations were static. We constructed 100 multivariate timeseries whose observations were each drawn from a single (stable) Gaussian distribution. For each dataset (indexed by m), we constructed a random covariance matrix, Σ_m :

$$\Sigma_m = \mathbf{C}\mathbf{C}^\top, \text{ where} \quad (11)$$

$$\mathbf{C}(i, j) \sim \mathcal{N}(0, 1), \text{ and where} \quad (12)$$

426 $i, j \in [1, 2, \dots, 50]$. In other words, all of the observations (for each of the 300 timepoints) within each dataset
427 were drawn from a multivariate Gaussian distribution with the same covariance matrix, and the 100 datasets
428 each used a different covariance matrix.

429 **Random.** We generated a second set of 100 synthetic datasets whose observations at each timepoint were
430 drawn from a Gaussian distribution with a new randomly constructed (using Eqn. 11) covariance matrix.
431 Because each timepoint’s covariance matrix was drawn independently from the covariance matrices for all
432 other timepoints, these datasets provided a test of reconstruction accuracy in the absence of any meaningful
433 underlying temporal structure in the dynamic correlations underlying the data.

Ramping. We generated a third set of 100 synthetic datasets whose underlying correlations changed gradually over time. For each dataset, we constructed two *anchor* “anchor” covariance matrices using Equation 11, Σ_{start} and Σ_{end} . For each of the 300 timepoints in each dataset, we drew the observations from a multivariate Gaussian distribution whose covariance matrix at each timepoint $t \in [0, \dots, 299]$ was given by

$$\Sigma_t = \left(1 - \frac{t}{299}\right) \Sigma_{\text{start}} + \frac{t}{299} \Sigma_{\text{end}}. \quad (13)$$

434 The gradually changing correlations underlying these datasets allow us to evaluate the recovery of dynamic
 435 correlations when each timepoint’s correlation matrix is unique (as in the random datasets), but where the
 436 correlation dynamics are structured and exhibit first-order autocorrelations (as in the constant datasets).

437 **Event.** We generated a fourth set of 100 synthetic datasets whose underlying correlation matrices exhibited
 438 prolonged intervals of stability, interspersed with abrupt changes. For each dataset, we used Equation 11
 439 to generate 5 random covariance matrices. We constructed a timeseries where each set of 60 consecutive
 440 samples was drawn from a Gaussian with the same covariance matrix. These datasets were intended to
 441 simulate a system that exhibits periods of stability punctuated by occasional abrupt state changes.

442 Synthetic data: simulating dynamic high-order correlations

443 We developed an iterative procedure for constructing timeseries data that exhibits known dynamic high-
 444 order correlations. The procedure builds on our approach to generating dynamic first-order correlations.
 445 Essentially, once we generate a timeseries with known first-order correlations, we can use the known first-
 446 order correlations as a template to generate a new timeseries of second-order correlations. In turn, we can
 447 generate a timeseries of third-order correlations from the second-order correlations, and so on. In general,
 448 we can generate order n correlations given a timeseries of order $n - 1$ correlations, for any $n > 1$. Finally,
 449 given the order n timeseries, we can reverse the preceding process to generate an order $n - 1$ timeseries, an
 450 order $n - 2$ order timeseries, and so on, until we obtain an order 0 timeseries of simulated data that reflects
 451 the chosen high-order dynamics.

452 The central mathematical operation in our procedure is the Kronecker product (\otimes). The Kronecker
 453 product of a $K \times K$ matrix, m_1 , with itself (i.e., $m_1 \otimes m_1$) produces a new $K^2 \times K^2$ matrix, m_2 whose entries reflect
 454 a scaled tiling of the entries in m_1 . If these tilings (scaled copies of m_1) are indexed by row and column, then
 455 the tile in the i^{th} row and j^{th} column contains the entries of m_1 , multiplied by $m_1(i, j)$. Following this pattern,
 456 the Kronecker product $m_2 \otimes m_2$ yields the $K^4 \times K^4$ matrix m_3 whose tiles are scaled copies of m_2 . In general,
 457 repeated applications of the Kronecker self-product may be used to generate $m_{n+1} = m_n \otimes m_n$ for $n > 1$, where

458 m_{n+1} is a $K^{2^n} \times K^{2^n}$ matrix. After generating a first-order timeseries of dynamic correlations (see *Synthetic*
459 *data: simulating dynamic first-order correlations*[Synthetic data: simulating dynamic first-order correlations](#)),
460 we use this procedure (applied independently at each timepoint) to transform it into a timeseries of n^{th} -order
461 correlations. When m_{n+1} is generated in this way, the temporal structure of the full timeseries (i.e., constant,
462 random, ramping, event) is preserved, since changes in the original first-order timeseries are also reflected
463 in the scaled tilings of itself that comprise the higher-order matrices.

464 Given a timeseries of n^{th} -order correlations, we then need to work “backwards” in order to generate the
465 order-zero timeseries. If the n^{th} -order correlation matrix at a given timepoint is m_n , then we can generate an
466 order $n - 1$ correlation matrix (for $n > 1$) by taking a draw from $\mathcal{N}(0, m_n)$ and reshaping the resulting vector
467 to have square dimensions. To force the resulting matrix to be symmetric, we remove its lower triangle, and
468 replace the lower triangle with (a reflected version of) its upper triangle. Intuitively, the *resulting* re-shaped
469 matrix will look like a noisy (but symmetric) version of the template matrix, m_{n-1} . (When $n = 1$, no re-
470 shaping is needed; the resulting K -dimensional vector may be used as the observation at the given timepoint.)
471 After independently drawing each timepoint’s order $n - 1$ correlation matrix from that timepoint’s order
472 n correlation matrix, this process can be applied repeatedly until $n = 0$. This results in a K -dimensional
473 timeseries of T observations containing the specified high-order correlations at orders 1 through n . Following
474 our approach to generating synthetic data exhibiting known first-order correlations, we constructed a total
475 of 400 additional multivariate timeseries, collectively reflecting a total of 4 qualitatively different patterns of
476 dynamic correlations (i.e., 100 datasets reflecting each type of dynamic pattern: constant, random, ramping,
477 and event). Each timeseries comprised 10 zero-order features (dimensions) that varied over 300 timepoints.
478 After applying our dynamic correlation estimation procedure, this yielded a 100-dimensional timeseries of
479 first-order features that could then be used to estimate dynamic second-order correlations. (We chose to
480 use $K = 10$ zero-order features for our higher order simulations in order to put the accuracy computations
481 displayed in Figs. 2 and 3 on a roughly even footing.)

482 Functional neuroimaging data collected during story listening

483 We examined an fMRI dataset collected by³⁶ that the authors have made publicly available at arks.princeton.edu/ark:/88435/ds
484 The dataset comprises neuroimaging data collected as participants listened to an audio recording of a story
485 (intact condition; 36 participants), listened to temporally scrambled recordings of the same story (17 partici-
486 pants in the paragraph-scrambled condition listened to the paragraphs in a randomized order and 36 in the
487 word-scrambled condition listened to the words in a randomized order), or lay resting with their eyes open
488 in the scanner (rest condition; 36 participants). Full neuroimaging details may be found in the original paper

489 for which the data were collected³⁶. Procedures were approved by the Princeton University Committee on
490 Activities Involving Human Subjects, and by the Western Institutional Review Board (Puyallup, WA). All
491 subjects were native English speakers with normal hearing and provided written informed consent.

492 **Hierarchical topographic factor analysis (HTFA).** Following our prior related work, we used HTFA¹¹
493 to derive a compact representation of the neuroimaging data. In brief, this approach approximates the
494 timeseries of voxel activations (44,415 voxels) using a much smaller number of radial basis function (RBF)
495 nodes in this case, 700 nodes, as determined by an optimization procedure described by¹¹. This provides
496 a convenient representation for examining full-brain network dynamics. All of the analyses we carried
497 out on the neuroimaging dataset were performed in this lower-dimensional space. In other words, each
498 participant's data matrix, X_0 , was a number-of-timepoints by 700 matrix of HTFA-derived factor weights
499 (where the row and column labels were matched across participants). Code for carrying out HTFA on fMRI
500 data may be found as part of the BrainIAK toolbox⁸⁸, which may be downloaded at brainiak.org.

501 **Temporal decoding**

502 We sought to identify neural patterns that reflected participants' ongoing cognitive processing of incoming
503 stimulus information. As reviewed by³⁶, one way of homing in on these stimulus-driven neural patterns
504 is to compare activity patterns across individuals (e.g., using ISFC analyses). In particular, neural patterns
505 will be similar across individuals to the extent that the neural patterns under consideration are stimulus-
506 driven, and to the extent that the corresponding cognitive representations are reflected in similar spatial
507 patterns across people also see⁵⁵. Following this logic, we used an across-participant temporal decoding test
508 developed by¹¹ to assess the degree to which different neural patterns reflected ongoing stimulus-driven
509 cognitive processing across people (Fig. 10). The approach entails using a subset of the data to train a
510 classifier to decode stimulus timepoints (i.e., moments in the story participants listened to) from neural
511 patterns. We use decoding (forward inference) accuracy on held-out data, from held-out participants, as a
512 proxy for the extent to which the inputted neural patterns reflected stimulus-driven cognitive processing in
513 a similar way across individuals.

514 **Forward inference and decoding accuracy**

515 We used an across-participant correlation-based classifier to decode which stimulus timepoint matched
516 each timepoint's neural pattern(Fig. 10. We first divided the participants into two groups: a template group,
517 $\mathcal{G}_{\text{template}}$ (i.e., training data), and a to-be-decoded group, $\mathcal{G}_{\text{decode}}$ (i.e., test data). We used Equation 7 to

518 compute a DISFC matrix for each group ($\bar{\mathbf{C}}_{\text{template}}$ and $\bar{\mathbf{C}}_{\text{decode}}$, respectively). We then correlated the rows of
519 $\bar{\mathbf{C}}_{\text{template}}$ and $\bar{\mathbf{C}}_{\text{decode}}$ to form a number-of-timepoints by number-of-timepoints decoding matrix, Λ . In this
520 way, the rows of Λ reflected timepoints from the template group, while the columns reflected timepoints
521 from the to-be-decoded group. We used Λ to assign temporal labels to each row $\bar{\mathbf{C}}_{\text{decode}}$ using the row of
522 $\bar{\mathbf{C}}_{\text{template}}$ with which it was most highly correlated. We then repeated this decoding procedure, but using
523 $\mathcal{G}_{\text{decode}}$ as the template group and $\mathcal{G}_{\text{template}}$ as the to-be-decoded group. Given the true timepoint labels
524 (for each group), we defined the *decoding accuracy* as the average proportion of correctly
525 decoded timepoints, across both groups. We defined the *relative decoding accuracy* as the difference between the decoding accuracy and chance accuracy (i.e., $\frac{1}{T}$).
526

527 Feature weighting and testing

528 We sought to examine which types of neural features (i.e., activations, first-order dynamic correlations, and
529 higher-order dynamic correlations) were informative to the temporal decoders. Using the notation above,
530 these features correspond to $\mathbf{X}_0, \mathbf{X}_1, \mathbf{X}_2, \mathbf{X}_3$, and so on.

531 [Figure 10 about here.]

532 One challenge to fairly evaluating high-order correlations is that if the kernel used in Equation 4 is
533 wider than a single timepoint, each repeated application of the equation will result in further temporal
534 blur. Because our primary assessment metric is temporal decoding accuracy, this unfairly biases against
535 detecting meaningful signal in higher-order correlations (relative to lower-order correlations). We attempted
536 to mitigate temporal blur in estimating each \mathbf{X}_n by using a Dirac δ function kernel (which places all of its
537 mass over a single timepoint; Fig. 9b, 10a) to compute each lower-order correlation ($\mathbf{X}_1, \mathbf{X}_2, \dots, \mathbf{X}_{n-1}$). We
538 then used a new (potentially wider, as described below) kernel to compute \mathbf{X}_n from \mathbf{X}_{n-1} . In this way,
539 temporal blurring was applied only in the last step of computing \mathbf{X}_n . We note that, because each \mathbf{X}_n is a
540 low-dimensional representation of the corresponding \mathbf{Y}_n , the higher-order correlations we estimated reflect
541 true correlations in the data with lower-fidelity than estimates of lower-order correlations. Therefore, even
542 after correcting for temporal blurring, our approach is still biased against finding meaningful signal in
543 higher-order correlations.

544 After computing each $\mathbf{X}_1, \mathbf{X}_2, \dots, \mathbf{X}_{n-1}$ for each participant, we divided participants into two equally sized
545 groups (± 1 for odd numbers of participants): $\mathcal{G}_{\text{train}}$ and $\mathcal{G}_{\text{test}}$. We then further subdivided $\mathcal{G}_{\text{train}}$ into $\mathcal{G}_{\text{train}_1}$
546 and $\mathcal{G}_{\text{train}_2}$. We then computed Λ (temporal correlation) matrices for each type of neural feature, using $\mathcal{G}_{\text{train}_1}$
547 and $\mathcal{G}_{\text{train}_2}$. This resulted in $n + 1$ Λ matrices (one for the original timeseries of neural activations, and one
548 for each of n orders of dynamic correlations). Our objective was to find a set of weights for each of these

549 Λ matrices such that the weighted average of the $n + 1$ matrices yielded the highest decoding accuracy.
550 We used quasi-Newton gradient ascent⁸⁹, using decoding accuracy (for $\mathcal{G}_{\text{train}_1}$ and $\mathcal{G}_{\text{train}_2}$) as the objective
551 function to be maximized, to find an optimal set of training data-derived weights, $\phi_{0,1,\dots,n}$, where $\sum_{i=0}^n \phi_i = 1$
552 and where $\phi_i \geq 0 \forall i \in [0, 1, \dots, n]$.

553 After estimating an optimal set of weights, we computed a new set of $n + 1$ Λ matrices correlating the
554 DISFC patterns from $\mathcal{G}_{\text{train}}$ and $\mathcal{G}_{\text{test}}$ at each timepoint. We use the resulting decoding accuracy of $\mathcal{G}_{\text{test}}$
555 timepoints (using the weights in $\phi_{0,1,\dots,n}$ to average the Λ matrices) to estimate how informative the set of
556 neural features containing up to n^{th} order correlations were.

557 We used a permutation-based procedure to form stable estimates of decoding accuracy for each set of
558 neural features. In particular, we computed the decoding accuracy for each of 10 random group assignments
559 of $\mathcal{G}_{\text{train}}$ and $\mathcal{G}_{\text{test}}$. We report the mean accuracy (along with 95% confidence intervals) for each set of neural
560 features.

561 Identifying robust decoding results

562 The temporal decoding procedure we use to estimate which neural features support ongoing cognitive
563 processing is governed by several parameters. In particular, Equation 4 requires defining a kernel function,
564 which can take on different shapes and widths. For a fixed set of neural features, each of these parameters
565 can yield different decoding accuracies. Further, the best decoding accuracy for a given timepoint may
566 be reliably achieved by one set of parameters, whereas the best decoding accuracy for another timepoint
567 might be reliably achieved by a different set of parameters, and the best decoding accuracy across *all* *all*
568 timepoints might be reliably achieved by still another different set of parameters. Rather than attempting
569 to maximize decoding accuracy, we sought to discover the trends in the data that were robust to classifier
570 parameters choices. Specifically, we sought to characterize how decoding accuracy varied (under different
571 experimental conditions) as a function of which neural features were considered.

572 To identify decoding results that were robust to specific classifier parameter choices, we repeated our
573 decoding analyses after substituting into Equation 4 each of a variety of kernel shapes and widths. We
574 examined Gaussian (Fig. 9c), Laplace (Fig. 9d), and Mexican Hat (Fig. 9e) kernels, each with widths of 5, 10,
575 20, and 50 samples. We then report the average decoding accuracies across all of these parameter choices.
576 This enabled us to (partially) factor out performance characteristics that were parameter-dependent, within
577 the set of parameters we examined.

578 **Reverse inference**

579 The dynamic patterns we examined comprise high-dimensional correlation patterns at each timepoint. To
580 help interpret the resulting patterns in the context of other studies, we created summary maps by computing
581 the across-timepoint average pairwise correlations at each order of analysis (first order, second order, etc.).
582 We selected the 10 strongest (absolute value) correlations at each order. Each correlation is between the
583 dynamic activity patterns (or patterns of dynamic high-order correlations) measured at two RBF nodes
584 (see *Hierarchical Topographic Factor Analysis*[Hierarchical Topographic Factor Analysis](#)). Therefore, the 10
585 strongest correlations involved up to 20 RBF nodes. Each RBF defines a spatial function whose activations
586 range from 0 to 1. We constructed a map of RBF components that denoted the endpoints of the 10 strongest
587 correlations (we set each RBF to have a maximum value of 1). We then carried out a meta analysis using
588 Neurosynth³⁸ to identify the 10 terms most commonly associated with the given map. This resulted in a set
589 of 10 terms associated with the average dynamic correlation patterns at each order.

590 **Data Availability**

591 The authors declare that the data supporting the findings of this study as well as the source data for
592 this paper are available at github.com/ContextLab/timecorr-paper/releases/tag/v0.4 and has been deposited
593 in the Zenodo database under accession code <https://doi.org/10.5281/zenodo.5165253>. The source data
594 underlying Figs. 2-6 and Supplementary Figs. S1-S9 are provided as a Source Data file. Source Data
595 are provided with the manuscript. The raw fMRI data are protected and are not available due to
596 data privacy laws. The processed fMRI dataset collected by ³⁶ has been made publicly available ⁹¹ at
597 arks.princeton.edu/ark:/88435/dsp015d86p269k.

598 **Code Availability**

599 All of our analysis code may be downloaded from github.com/ContextLab/timecorr-paper/releases/tag/v0.4.
600 We have also published a companion Python toolbox that may be downloaded from timecorr.readthedocs.io.

602 **Acknowledgements**

603 We acknowledge discussions with Luke Chang, Vassiki Chauhan, Hany Farid, Paxton Fitzpatrick, Andrew
604 Heusser, Eshin Jolly, Aaron Lee, Qiang Liu, Matthijs van der Meer, Judith Mildner, Gina Notaro, Stephen

605 Satterthwaite, Emily Whitaker, Weizhen Xie, and Kirsten Ziman. Our work was supported in part by NSF
606 EPSCoR Award Number 1632738 to J.R.M. and by a sub-award of DARPA RAM Cooperative Agreement
607 N66001-14-2-4-032 to J.R.M. The content is solely the responsibility of the authors and does not necessarily
608 represent the official views of our supporting organizations.

609 **Author contributions**

610 Concept: J.R.M. Implementation: T.H.C., L.L.W.O., and J.R.M. Analyses: L.L.W.O. and J.R.M. Writing:
611 L.L.W.O. and J.R.M.

612 **Competing interests**

613 The authors declare no competing interests.

614 **References**

- 615 [1] Haxby, J. V. et al. Distributed and overlapping representations of faces and objects in ventral temporal cortex.
616 Science **293**, 2425–2430 (2001).
- 617 [2] Norman, K. A., Polyn, S. M., Detre, G. J. & Haxby, J. V.
618 Beyond mind-reading: multi-voxel pattern analysis of fMRI data. Trends in Cognitive Sciences **10**,
619 424–430 (2006).
- 620 [3] Tong, F. & Pratte, M. S. Decoding patterns of human brain activity. Annual Review of Psychology **63**,
621 483–509 (2012).
- 622 [4] Mitchell, T. M. et al. Predicting human brain activity associated with the meanings of nouns. Science
623 320, 1191 (2008).
- 624 [5] Kamitani, Y. & Tong, F. Decoding the visual and subjective contents of the human brain.
625 Nature Neuroscience **8**, 679–685 (2005).
- 626 [6] Nishimoto, S. et al. Reconstructing visual experience from brain activity evoked by natural movies.
627 Current Biology **21**, 1–6 (2011).
- 628 [7] Pereira, F. et al. Toward a universal decoder of linguistic meaning from brain activation.
629 Nature Communications **9**, 1–13 (2018).

- 630 [8] Huth, A. G., Nisimoto, S., Vu, A. T. & Gallant, J. L. A continuous semantic space describes the representation of thousands of natural scenes. *Neuron* **76**, 1210–1224 (2012).
- 631
- 632 [9] Huth, A. G., de Heer, W. A., Griffiths, T. L., Theunissen, F. E. & Gallant, J. L. Natural speech reveals the semantic maps that tile human cerebral cortex. *Nature* **532**, 453–458 (2016).
- 633
- 634
- 635 [10] Etzel, J. A., Gazzola, V. & Keysers, C. An introduction to anatomical ROI-based fMRI classification. *Brain Research* **1281**, 114–125 (2009).
- 636
- 637 [11] Manning, J. R. *et al.* A probabilistic approach to discovering dynamic full-brain functional connectivity patterns. *NeuroImage* **180**, 243–252 (2018).
- 638
- 639 [12] Fong, A. H. C. *et al.* Dynamic functional connectivity during task performance and rest predicts individual differences in cognitive control. *NeuroImage* **188**, 14–25 (2019).
- 640
- 641 [13] Grossberg, S. Nonlinear neural networks: principles, mechanisms, and architectures. *Neural Networks* **1**, 17–61 (1988).
- 642
- 643 [14] Friston, K. J. The labile brain. I. neuronal transients and nonlinear coupling. *Philosophical Transactions of the Royal Society of London* **355B**, 215–236 (2000).
- 644
- 645 [15] Sporns, O. & Honey, C. J. Small worlds inside big brains. *Proceedings of the National Academy of Sciences, USA* **103**, 19219–19220 (2006).
- 646
- 647 [16] Bassett, D., Meyer-Lindenberg, A., Achard, S., Duke, T. & Bullmore, E. Adaptive reconfiguration of fractal small-world human brain functional networks. *Proceedings of the National Academy of Sciences, USA* **103**, 19518–19523 (2006).
- 648
- 649
- 650 [17] Turk-Browne, N. B. Functional interactions as big data in the human brain. *Science* **342**, 580–584 (2013).
- 651
- 652 [18] Demertzi, A. *et al.* Human consciousness is supported by dynamic complex patterns of brain signal coordination. *Science Advances* **5**, eaat7603 (2019).
- 653
- 654 [19] Solomon, S. H., Medaglia, J. D. & Thompson-Schill, S. L. Implementing a concept network model. *Behavior Research Methods* **51**, 1717–1736 (2019).
- 655
- 656 [20] Lurie, D. *et al.* On the nature of time-varying functional connectivity in resting fMRI. *PsyArXiv* doi.org/10.31234/osf.io/xtzre (2018).
- 657

- 658 [21] Preti, M. G., Bolton, T. A. W. & Van De Ville, D. The dynamic functional connectome: state-of-the-art and perspectives.
659 *NeuroImage* **160**, 41–54 (2017).
- 660 [22] Zou, Y., Donner, R. V., Marwan, N., Donges, J. F. & Kurths, J.
661 Complex network approaches to nonlinear time series analysis. *Physics Reports* **787**, 1–97 (2019).
- 662
- 663 [23] Mack, M. L., Preston, A. R. & Love, B. C. Medial prefrontal cortex compresses concept representations through learning
664 *bioRxiv* doi.org/10.1101/178145 (2017).
- 665 [24] Bressler, S. L. & Kelso, J. A. S. Cortical coordination dynamics and cognition.
666 *Trends in Cognitive Sciences* **5**, 26–36 (2001).
- 667 [25] McIntosh, A. R. Towards a network theory of cognition. *Neural Networks* **13**, 861–870 (2000).
- 668 [26] Reimann, M. W. *et al.* Cliques of neurons bound into cavities provide a missing link between structure and function.
669 *Frontiers in Computational Neuroscience* **11**, 1–16 (2017).
- 670 [27] Beaty, R. E., Benedek, M., Silvia, P. J. & Schacter, D. L. Creative cognition and brain network dynamics.
671 *Trends in Cognitive Sciences* **20**, 87–95 (2016).
- 672 [28] Bullmore, E. & Sporns, O. Complex brain networks: graph theoretical analysis of structural and functional systems.
673 *Nature Reviews Neuroscience* **10**, 186–198 (2009).
- 674 [29] Pearson, K. On lines and planes of closest fit to systems of points in space.
675 *The London, Edinburgh, and Dublin Philosophical Magazine and Journal of Science* **2**, 559–572 (1901).
- 676
- 677 [30] McIntosh, A. R. & Jirsa, V. K. The hidden repertoire of brain dynamics and dysfunction.
678 *Network Neuroscience* doi.org/10.1162/netn_a_00107 (2019).
- 679 [31] Toker, D. & Sommer, F. T. Information integration in large brain networks. *PLoS Computational Biology*
680 **15**, e1006807 (2019).
- 681 [32] Gonzalez-Castillo, J. *et al.* Imaging the spontaneous flow of thought: distinct periods of cognition contribute to dynamical
682 *NeuroImage* **202** (2019).
- 683 [33] Landau, E. Zur relativen Wertbemessung der Turnierresultate. *Deutsches Wochenschach* **11**, 366–369
684 (1895).

- 685 [34] Betzel, R. F., Byrge, L., Esfahlani, F. Z. & Kennedy, D. P.
686 Temporal fluctuations in the brain's modular architecture during movie-watching. *bioRxiv*
687 doi.org/10.1101/750919 (2019).
- 688 [35] Sizemore, A. E. et al. Cliques and cavities in the human connectome.
689 *Journal of Computational Neuroscience* **44**, 115–145 (2018).
- 690 [36] Simony, E., Honey, C. J., Chen, J. & Hasson, U. Dynamic reconfiguration of the default mode network during narrative
691 *Nature Communications* **7**, 1–13 (2016).
- 692 [37] Hasson, U., Yang, E., Vallines, I., Heeger, D. J. & Rubin, N.
693 A hierarchy of temporal receptive windows in human cortex. *The Journal of Neuroscience* **28**, 2539–2550
694 (2008).
- 695 [38] Rubin, T. N. et al. Decoding brain activity using a large-scale probabilistic functional-anatomical atlas of human cognition.
696 *PLoS Computational Biology* **13**, e1005649 (2017).
- 697 [39] Park, H.-J., Friston, K. J., Pae, C., Park, B. & Razi, A. Dynamic effective connectivity in resting state fMRI.
698 *NeuroImage* **180**, 594–608 (2018).
- 699 [40] Roy, D. S. et al. Brain-wide mapping of contextual fear memory engram ensembles supports the dispersed engram com
700 *bioRxiv* doi.org/10.1101/668483 (2019).
- 701 [41] Liégeois, R. et al. Resting brain dynamics at different timescales capture distinct aspects of human behavior.
702 *Nature Communications* **10**, 1–9 (2019).
- 703 [42] Chang, C. & Glover, G. H. Time-frequency dynamics of resting-state brain connectivity measured with fMRI.
704 *NeuroImage* **50**, 81–98 (2010).
- 705 [43] Zheng, M., Allard, A., Hagmann, P. & Serrano, M. . . A. Geometric renormalization unravels self-similarity of the multi
706 *arXiv* **1904.11793** (2019).
- 707 [44] Baldassano, C. et al. Discovering event structure in continuous narrative perception and memory.
708 *Neuron* **95**, 709–721 (2017).
- 709 [45] Hasson, U., Chen, J. & Honey, C. J. Hierarchical process memory: memory as an integral component of information pro
710 *Trends in Cognitive Sciences* **19**, 304–315 (2015).
- 711 [46] Honey, C. J. et al. Slow cortical dynamics and the accumulation of information over long timescales.
712 *Neuron* **76**, 423–434 (2012).

- 713 [47] Lerner, Y., Honey, C. J., Silbert, L. J. & Hasson, U. Topographic mapping of a hierarchy of temporal receptive windows using fMRI. *The Journal of Neuroscience* **31**, 2906–2915 (2011).
- 714
- 715 [48] Lerner, Y., Honey, C. J., Katkov, M. & Hasson, U. Temporal scaling of neural responses to compressed and dilated natural sounds. *Journal of Neurophysiology* **111**, 2433–2444 (2014).
- 716
- 717 [49] Chien, H.-Y. S. & Honey, C. J. Constructing and forgetting temporal context in the human cerebral cortex. *bioRxiv* doi.org/10.1101/761593 (2019).
- 718
- 719 [50] Lee, C. S., Aly, M. & Baldassano, C. Anticipation of temporally structured events in the brain. *bioRxiv* [10.1101/2020.10.14.338145](https://doi.org/10.1101/2020.10.14.338145) (2020).
- 720
- 721 [51] Fallon, J., Ward, P. G. D., Parkes, L. & Oldham, S. Timescales of spontaneous fMRI fluctuations relate to structural connectivity. *Network Neuroscience* **4**, 788–806 (2020).
- 722
- 723 [52] Shappell, H., Caffo, B. S., Pekar, J. J. & Lindquist, M. A. Improved state change estimation in dynamic functional connectivity. *NeuroImage* **191**, 243–257 (2019).
- 724
- 725 [53] Vidaurre, D. *et al.* Discovering dynamic brain networks from big data in rest and task. *NeuroImage* **180**, 646–656 (2018).
- 726
- 727 [54] Allen, E. A. *et al.* Tracking whole-brain connectivity dynamics in the resting state. *Cerebral Cortex* **24**, 663–676 (2012).
- 728
- 729 [55] Simony, E. & Chang, C. Analysis of stimulus-induced brain dynamics during naturalistic paradigms. *NeuroImage* **216**, 116461 (2020).
- 730
- 731 [56] Zar, J. H. *Biostatistical analysis* (Prentice-Hall, 2010).
- 732 [57] Tipping, M. E. & Bishop, C. M. Probabilistic principal component analysis. *Journal of Royal Statistical Society, Series B* **61**, 611–622 (1999).
- 733
- 734 [58] Spearman, C. General intelligence, objectively determined and measured. *American Journal of Psychology* **15**, 201–292 (1904).
- 735
- 736 [59] Jutten, C. & Herault, J. Blind separation of sources, part I: an adaptive algorithm based on neuromimetic architecture. *Signal Processing* **24**, 1–10 (1991).
- 737
- 738 [60] Comon, P., Jutten, C. & Herault, J. Blind separation of sources, part II: problems statement. *Signal Processing* **24**, 11–20 (1991).
- 739

- 740 [61] van der Maaten, L. J. P. & Hinton, G. E. Visualizing high-dimensional data using t-SNE.
741 *Journal of Machine Learning Research* **9**, 2579–2605 (2008).
- 742 [62] McInnes, L., Healy, J. & Melville, J. UMAP: uniform manifold approximation and projection for dimension reduction.
743 *arXiv* **1802** (2018).
- 744 [63] Lee, D. D. & Seung, H. S. Learning the parts of objects by non-negative matrix factorization. *Nature*
745 **401**, 788–791 (1999).
- 746 [64] Manning, J. R., Ranganath, R., Norman, K. A. & Blei, D. M.
747 Topographic factor analysis: a Bayesian model for inferring brain networks from neural data.
748 *PLoS One* **9**, e94914 (2014).
- 749 [65] Gershman, S. J., Blei, D. M., Pereira, F. & Norman, K. A.
750 A topographic latent source model for fMRI data. *NeuroImage* **57**, 89–100 (2011).
- 751 [66] Mairal, J. B., Bach, F., Ponce, J. & Sapiro, G. Online dictionary learning for sparse coding.
752 *Proceedings of the International Conference on Machine Learning* 689–696 (2009).
- 753 [67] Mairal, J., Ponce, J., Sapiro, G., Zisserman, A. & Bach, F. R. Supervised dictionary learning.
754 *Advances in Neural Information Processing Systems* 1033–1040 (2009).
- 755 [68] Hinton, G. E. & Salakhutdinov, R. R. Reducing the dimensionality of data with neural networks.
756 *Science* **313**, 504–507 (2006).
- 757 [69] Newman, M. E. J. A measure of betweenness centrality based on random walks. *Social Networks* **27**,
758 39–54 (2005).
- 759 [70] Opsahl, T., Agneessens, F. & Skvoretz, J. Node centrality in weighted networks: generalizing degree and shortest paths
760 *Social Networks* **32**, 245–251 (2010).
- 761 [71] Barthélemy, M. Betweenness centrality in large complex networks. *European Physical Journal B* **38**,
762 163–168 (2004).
- 763 [72] Geisberger, R., Sanders, P. & Schultes, D. Better approximation of betweenness centrality.
764 *Proceedings of the Meeting on Algorithm Engineering and Experiments* 90–100 (2008).
- 765 [73] Freeman, L. C. A set of measures of centrality based on betweenness. *Sociometry* **40**, 35–41 (1977).
- 766 [74] Rao, C. R. Diversity and dissimilarity coefficients: a unified approach. *Theoretical Population Biology* **21**,
767 24–43 (1982).

- 768 [75] Lin, J. Divergence measures based on the Shannon entropy. *IEEE Transactions on Information Theory* **37**,
769 145–151 (2009).
- 770 [76] Ricotta, C. & Szeidl, L. Towards a unifying approach to diversity measures: bridging the gap between the Shannon ent
771 *Theoretical Population Biology* **70**, 237–243 (2006).
- 772 [77] Newman, M. E. J. The mathematics of networks. *The New Palgrave Encyclopedia of Economics* **2**, 1–12
773 (2008).
- 774 [78] Bonacich, P. Some unique properties of eigenvector centrality. *Social Networks* **29**, 555–564 (2007).
- 775 [79] Lohmann, G. et al. Eigenvector centrality mapping for analyzing connectivity patterns in fMRI data of the human brain.
776 *PLoS One* **5**, e10232 (2010).
- 777 [80] Halu, A., Mondragón, R. J., Panzarasa, P. & Bianconi, G. Multiplex PageRank. *PLoS One* **8**, e78293
778 (2013).
- 779 [81] Honey, C. J., Kötter, R., Breakspear, M. & Sporns, O. Network structure of cerebral cortex shapes functional connectivity
780 *Proceedings of the National Academy of Sciences, USA* **104**, 10240–10245 (2007).
- 781 [82] Schreiber, T. Measuring information transfer. *Physical Review Letters* **85**, 461–464 (2000).
- 782 [83] Alvarez-Hamelin, I., Dall'Asta, L., Barrat, A. & Vespignani, A.
783 k-corr decomposition: a tool for the visualization of large scale networks. *arXiv cs/0504107v2* (2005).
- 784 [84] Christakis, N. A. & Fowler, J. H. Social network sensors for early detection of contagious outbreaks.
785 *PLoS One* **5**, e12948 (2010).
- 786 [85] Rubinov, M. & Sporns, O. Complex network measures of brain connectivity: uses and interpretations.
787 *NeuroImage* **52**, 1059–1069 (2010).
- 788 [86] Estrada, E. & Rodríguez-Velázquez, J. A. Subgraph centrality in complex networks. *Physical Review E*
789 **71**, 056103 (2005).
- 790 [87] Thompson, W. H., Richter, C. G., Plavén-Sigray, P. & Fransson, P.
791 Simulations to benchmark time-varying connectivity methods for fMRI. *PLoS Computational Biology*
792 **14**, e1006196 (2018).
- 793 [88] Capota, M. et al. Brain imaging analysis kit (2017).
- 794 [89] Nocedal, J. & Wright, S. J. *Numerical optimization* (Springer, New York, NY, 2006).

- 795 [90] Combrisson, E. *et al.* Visbrain: a multi-purpose GPU-accelerated open-source suite for multimodal brain data visualization. *Frontiers in Neuroinformatics* **13**, 1–14 (2019).
- 796
- 797 [91] Simony, E., Honey, C. J., Chen, J. & Hasson, U. Dynamic reconfiguration of the default mode network during narrative processing. *DataSpace* <http://arks.princeton.edu/ark:/88435/dsp015d86p269k> (2016).
- 798

⁷⁹⁹ **Figures**

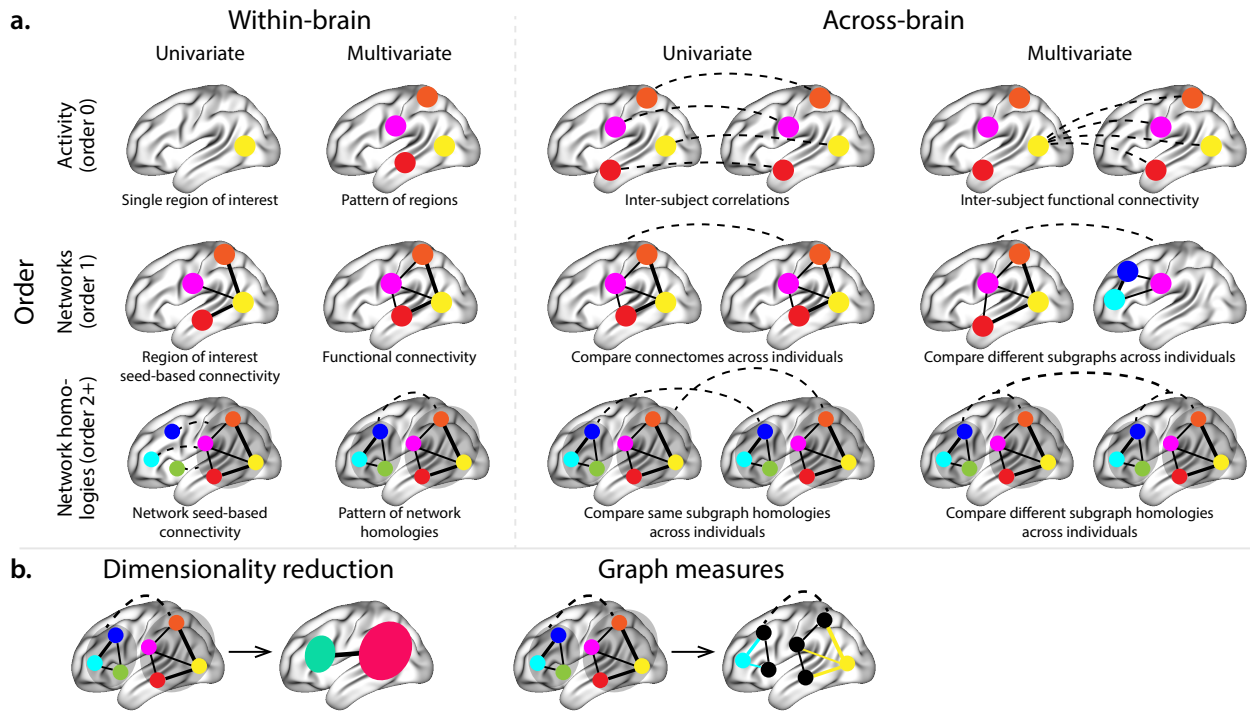


Figure 1: Neural patterns. a. A space of neural features. Within-brain analyses are carried out within a single brain, whereas across-brain analyses compare neural patterns across two or more individuals' brains. Univariate analyses characterize the activities of individual units (e.g., nodes, small networks, hierarchies of networks, etc.), whereas multivariate analyses characterize the patterns of activity across units. Order 0 patterns involve individual nodes; order 1 patterns involve node-node interactions; order 2 (and higher) patterns relate to interactions between homologous networks. Each of these patterns may be static (e.g., averaging over time) or dynamic. **b. Summarizing neural patterns.** To efficiently compute with complex neural patterns, it can be useful to characterize the patterns using summary measures. Dimensionality reduction algorithms project the patterns onto lower-dimensional spaces whose dimensions reflect weighted combinations or non-linear transformations of the dimensions in the original space. Graph measures characterize each unit's participation in its associated network.

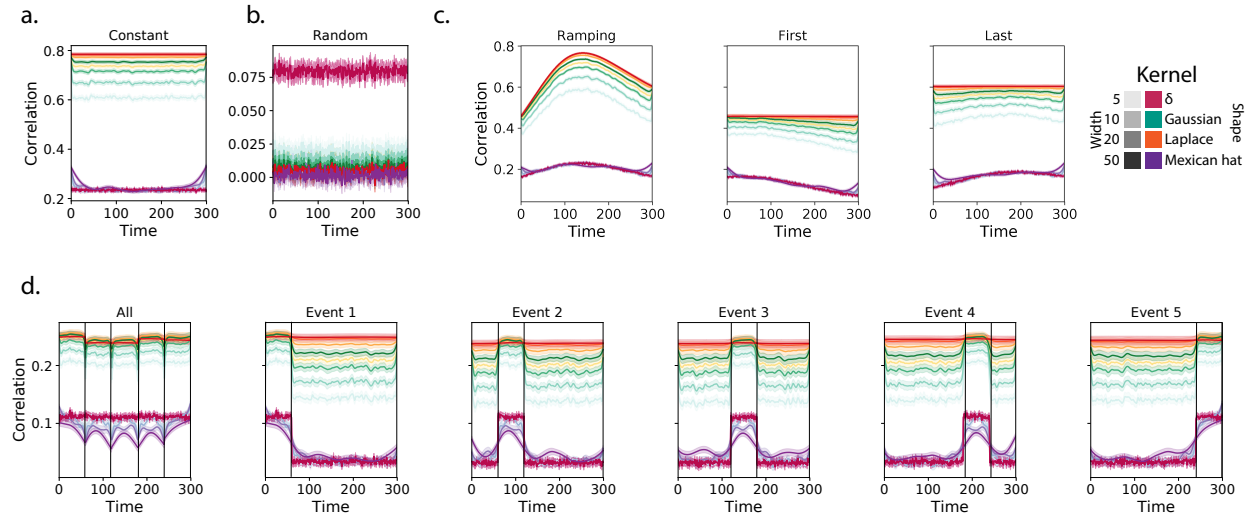


Figure 2: Recovering known dynamic first-order correlations from synthetic data. Each panel displays the average correlations between the vectorized upper triangles of the recovered correlation matrix at each timepoint and either the true underlying correlation at each timepoint or a reference correlation matrix. (The averages are taken across 100 different randomly generated synthetic datasets of each given category, each with $K = 50$ features and $T = 300$ timepoints.) Error ribbons denote 95% confidence intervals [of the mean](#) (taken across datasets). Different colors denote different kernel shapes, and the shading within each color family denotes the kernel width parameter. For a complete description of each synthetic dataset, see [Synthetic data: simulating dynamic first-order correlations](#) [Synthetic data: simulating dynamic first-order correlations](#).

a. Constant correlations. These datasets have a stable (unchanging) underlying correlation matrix.

b. Random correlations. These datasets are generated using a new independently drawn correlation matrix at each new timepoint.

c. Ramping correlations. These datasets are generated by smoothly varying the underlying correlations between the randomly drawn correlation matrices at the first and last timepoints. The left panel displays the correlations between the recovered dynamic correlations and the underlying ground truth correlations. The middle panel compares the recovered correlations with the [first](#) [first](#) timepoint's correlation matrix. The right panel compares the recovered correlations with the [last](#) [last](#) timepoint's correlation matrix.

d. Event-based correlations. These datasets are each generated using five randomly drawn correlation matrices that each remain stable for a fifth of the total timecourse. The left panel displays the correlations between the recovered dynamic correlations and the underlying ground truth correlations. The right panels compare the recovered correlations with the correlation matrices unique to each event. The vertical lines denote event boundaries. [Source data are provided as a Source Data file](#).

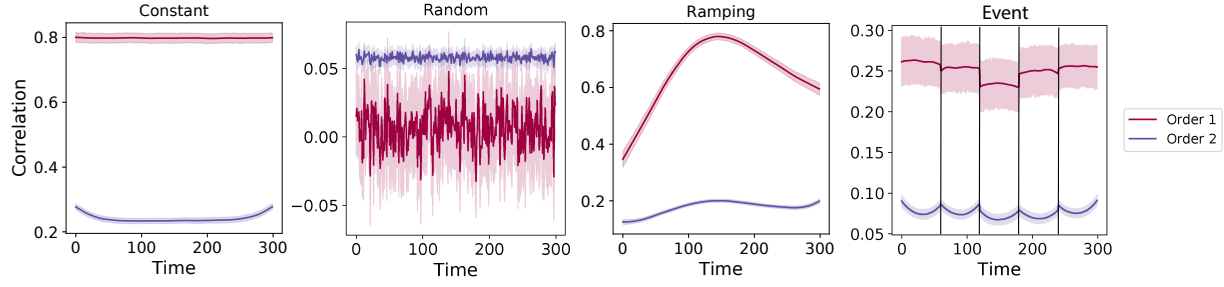


Figure 3: Recovery of simulated first-order and second-order dynamic correlations. Each panel displays the average correlations between the vectorized upper triangles of the recovered first-order and second-order correlation matrices and the true (simulated) first-order and second order correlation matrices at each timepoint and for each synthetic dataset. (The averages are taken across 100 different randomly generated synthetic datasets of each given category, each with $K = 10$ features and $T = 300$ timepoints.) Error ribbons denote 95% confidence intervals of the mean (taken across datasets). For a complete description of each synthetic dataset, see [Synthetic data: simulating dynamic higher-order correlations](#). All estimates represented in this figure were computed using a Laplace kernel (width = 20). **Constant.** These datasets have stable (unchanging) underlying second-order correlation matrices. **Random.** These datasets are generated using a new independently drawn second-order correlation matrix at each timepoint. **Ramping.** These datasets are generated by smoothly varying the underlying second-order correlations between the randomly drawn correlation matrices at the first and last timepoints. **Event.** These datasets are each generated using five randomly drawn second-order correlation matrices that each remain stable for a fifth of the total timecourse. The vertical lines denote event boundaries. Note that the “dips” and “ramps” at the boundaries of sharp transitions (e.g., the beginning and ends of the “constant” and “ramping” datasets, and at the event boundaries of the “event” datasets) are finite-sample effects that reflect the reduced numbers of samples that may be used to accurately estimate correlations at sharp boundaries. [Source data are provided as a Source Data file](#).

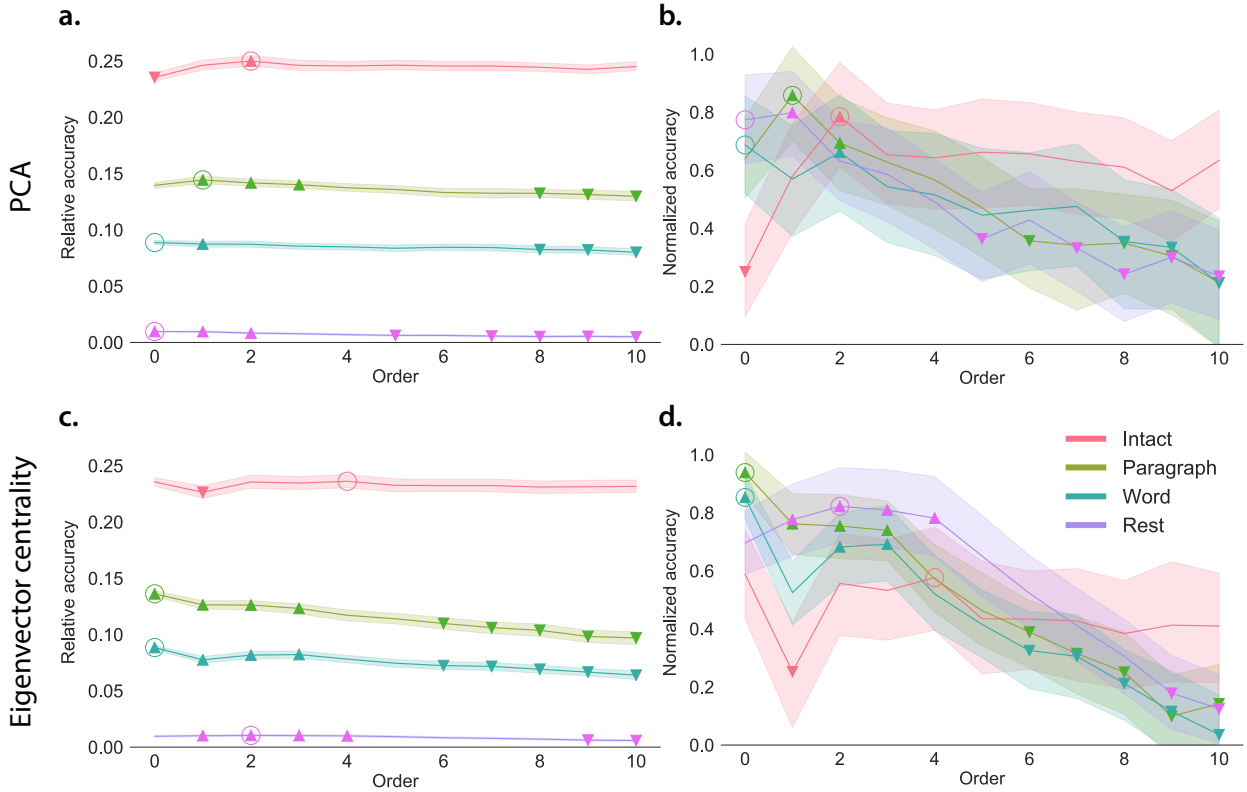


Figure 4: Across-participant timepoint decoding accuracy varies with correlation order and cognitive engagement. **a. Decoding accuracy as a function of order: PCA.** Order “Order” (x-axis) refers to the maximum order of dynamic correlations that were available to the classifiers (see [Feature weighting and testing](#)). The reported across-participant decoding accuracies are averaged over all kernel shapes and widths (see [Identifying robust decoding results](#)). The y-values are displayed relative to chance accuracy (intact: $\frac{1}{300}$; paragraph: $\frac{1}{272}$; word: $\frac{1}{300}$; rest: $\frac{1}{400}$; these chance accuracies were subtracted from the observed accuracies to obtain the relative accuracies reported on the y-axis). The error ribbons denote 95% confidence intervals of the means across cross-validation folds (i.e., random assignments of participants to the training and test sets). The colors denote the experimental condition. Arrows denote sets of features that yielded reliably higher (upward facing) or lower (downward facing) decoding accuracy than the mean of all other features (via a two-tailed t -test, thresholded at $p < 0.05$). Figure 5 displays additional comparisons between the decoding accuracies achieved using different sets of neural features. The circled values represent the maximum decoding accuracy within each experimental condition. **b. Normalized timepoint decoding accuracy as a function of order: PCA.** This panel displays the same results as Panel a, but here each curve has been normalized to be bounded between 0 and have a maximum value of 1 (inclusive) by subtracting the minimum accuracy value of 0 (across all folds and orders) and then dividing by including the maximum accuracy (again, across all folds upper and orders lower bounds of the respective 95% confidence intervals of the mean). Panels a and b used PCA to project each high-dimensional pattern of dynamic correlations onto a lower-dimensional space. **c. Timepoint decoding accuracy as a function of order: eigenvector centrality.** This panel is in the same format as Panel a, but here eigenvector centrality has been used to project the high-dimensional patterns of dynamic correlations onto a lower-dimensional space. **d. Normalized timepoint decoding accuracy as a function of order: eigenvector centrality.** This panel is in the same format as Panel b, but here eigenvector centrality has been used to project the high-dimensional patterns of dynamic correlations onto a lower-dimensional space. See Figures S1 and S2 for decoding results broken down by kernel shape and width, respectively. [Source data are provided as a Source Data file](#).

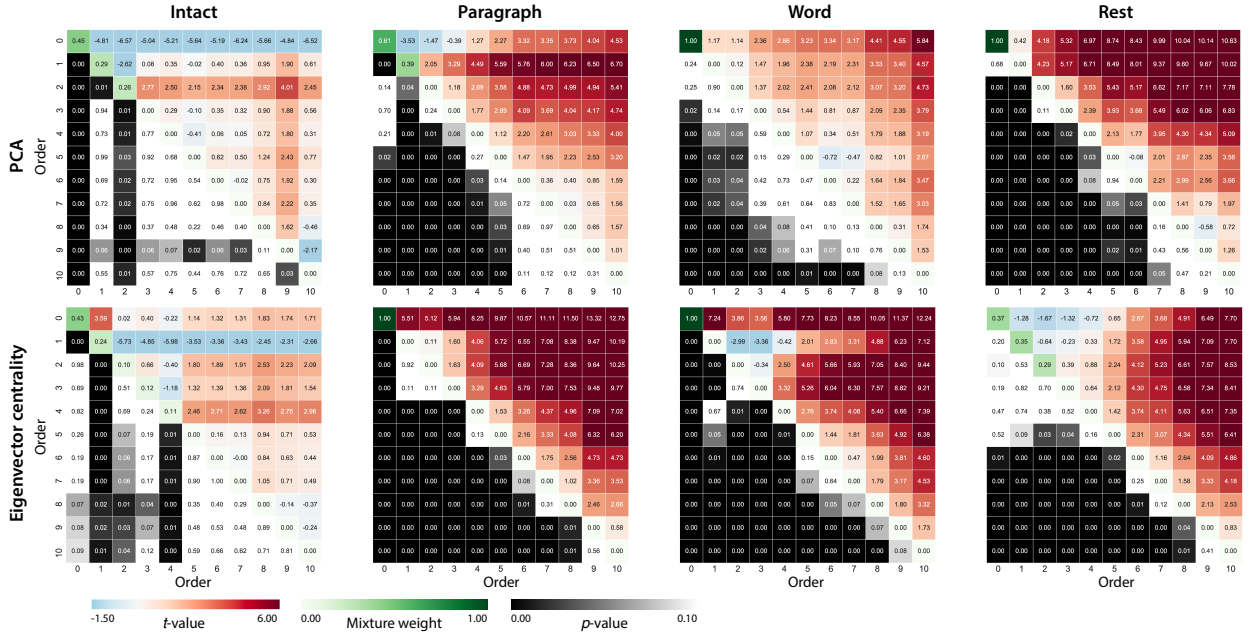


Figure 5: Statistical summary of decoding accuracies for different neural features. Each column of matrices displays decoding results for one experimental condition (intact, paragraph, word, and rest). We considered dynamic activity patterns (order 0) and dynamic correlations at different orders (order > 0). We used two-tailed t -tests to compare the distributions of decoding accuracies obtained using each pair of features. The distributions for each feature reflect the set of average decoding accuracies (across all kernel parameters), obtained for each random assignment of training and test groups. In the upper triangles of each matrix, warmer colors (positive t -values) indicate that the neural feature indicated in the given row yielded higher accuracy than the feature indicated in the given column. Cooler colors (negative t -values) indicate that the feature in the given row yielded lower decoding accuracy than the feature in the given column. The lower triangles of each map denote the corresponding p -values for the t -tests. The diagonal entries display the relative average optimized weight given to each type of feature in a decoder that included all feature types (see [Feature weighting and testing](#)).

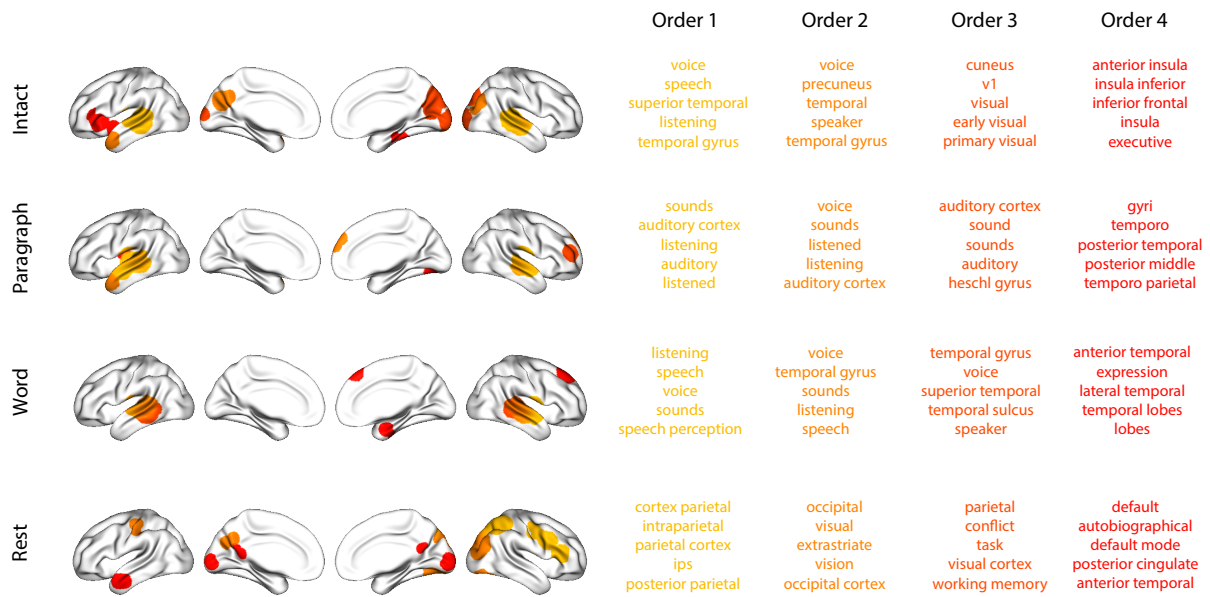


Figure 6: Top terms associated with the most strongly correlated nodes at each order. Each color corresponds to one order of inter-subject functional correlations. To calculate the dynamic correlations, eigenvector centrality has been used to project the high-dimensional patterns of dynamic correlations onto a lower-dimensional space at each previous order, which allows us to map the brain regions at each order by retaining the features of the original space. The inflated brain plots display the locations of the endpoints of the 10 strongest (absolute value) correlations at each order, thresholded at 0.999, and projected onto the cortical surface⁹⁰. The lists of terms on the right display the top five Neurosynth terms³⁸ decoded from the corresponding brain maps for each order. Each row displays data from a different experimental condition. Additional maps and their corresponding Neurosynth terms may be found in the [Supplementary materials](#) (intact: Fig. S5; paragraph: Fig. S6; word: Fig. S7; rest: Fig. S8). Source data are provided as a [Source Data file](#).

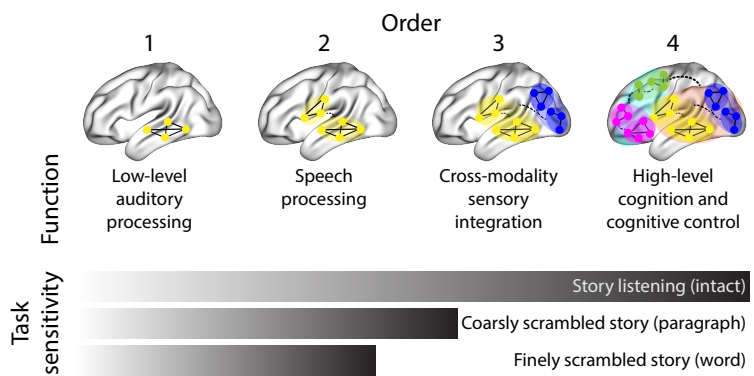


Figure 7: Proposed high-order network dynamics underlying high-level cognition during story listening. Schematic depicts higher orders of network interactions supporting higher-level aspects of cognitive processing. When tasks evoke richer, deeper, and/or higher-level processing, this is reflected in higher-order network interactions.

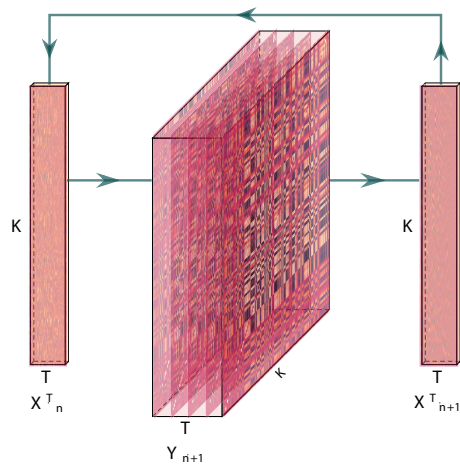


Figure 8: Estimating dynamic high-order correlations. Given a T by K matrix of multivariate timeseries data, \mathbf{X}_n (where $n \in \mathbb{N}, n \geq 0$), we use Equation 4 to compute a timeseries of K by K correlation matrices, \mathbf{Y}_{n+1} . We then approximate \mathbf{Y}_{n+1} with the T by K matrix \mathbf{X}_{n+1} . This process may be repeated to scalably estimate iteratively higher-order correlations in the data. Note that the transposes of \mathbf{X}_n and \mathbf{X}_{n+1} are displayed in the figure for compactness.

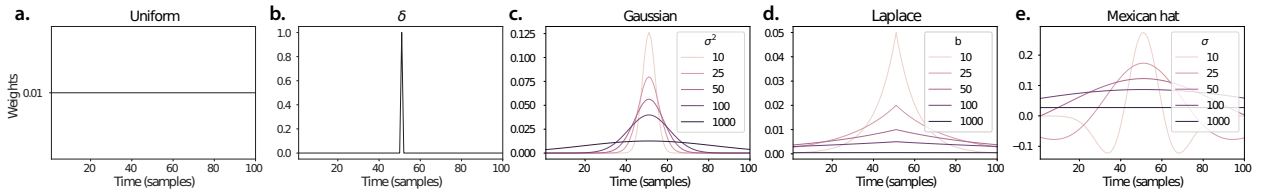


Figure 9: Examples of kernel functions. Each panel displays per-timepoint weights for a kernel centered at $t = 50$, evaluated at 100 timepoints ($\tau \in [1, \dots, 100]$). **a. Uniform kernel.** The weights are timepoint-invariant; observations at all timepoints are weighted equally, and do not change as a function of τ . This is a special case kernel function that reduces dynamic correlations to static correlations. **b. Dirac δ kernel.** Only the observation at timepoint t is given a non-zero weight (of 1). **c. Gaussian kernels.** Each kernel's weights fall off in time according to a Gaussian probability density function centered on time t . Weights derived using several different example width parameters (σ^2) are displayed. **d. Laplace kernels.** Each kernel's weights fall off in time according to a Laplace probability density function centered on time t . Weights derived using several different example width parameters (b) are displayed. **e. Mexican hat (Ricker wavelet) kernels.** Each kernel's weights fall off in time according to a Ricker wavelet centered on time t . This function highlights the contrasts between local versus surrounding activity patterns in estimating dynamic correlations. Weights derived using several different example width parameters (σ) are displayed.

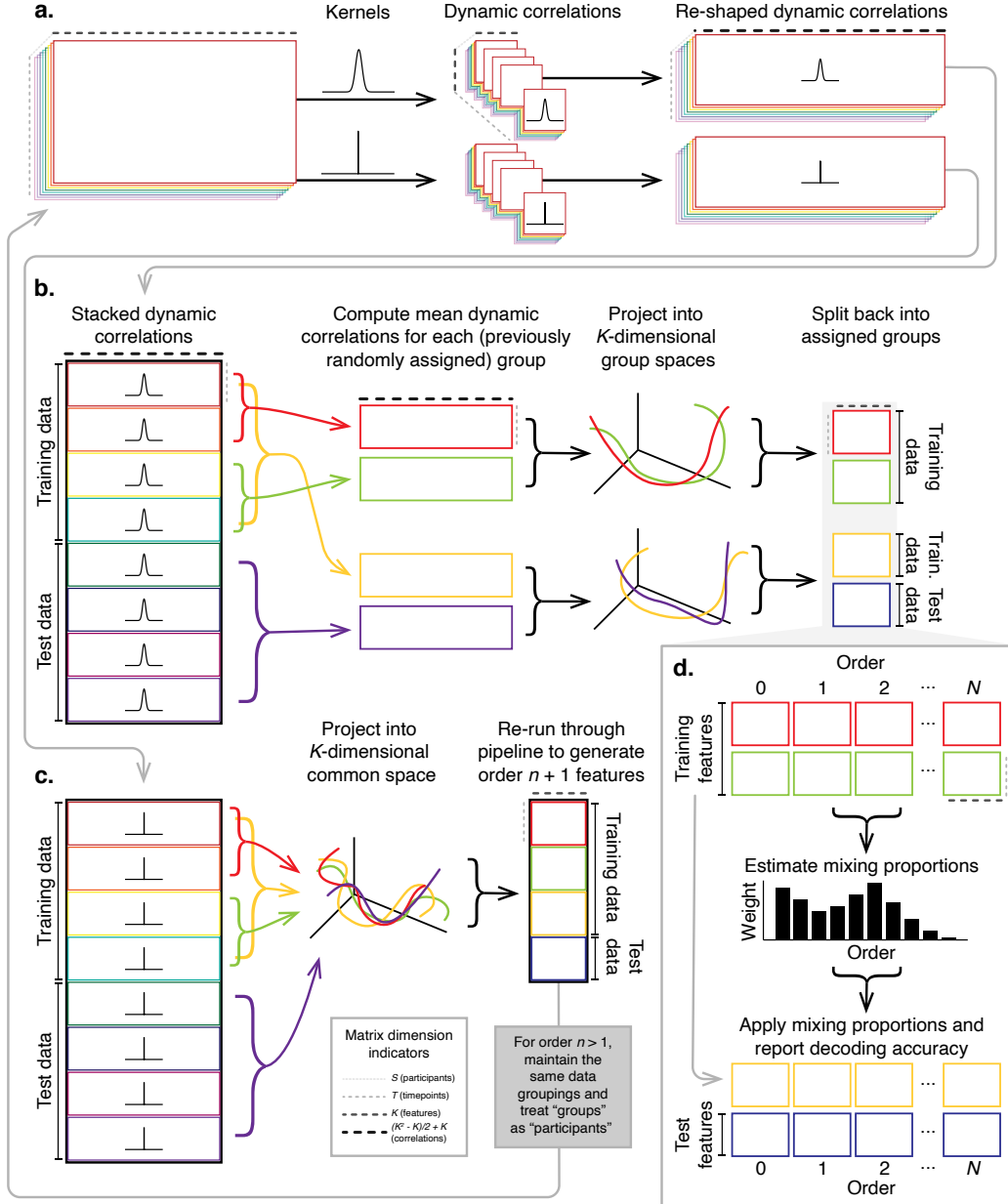


Figure 10: Decoding analysis pipeline. **a. Computing dynamic correlations from timeseries data.** Given a timeseries of observations as a $T \times K$ matrix (or a set of S such matrices), we use Equation 4 to compute each participant's DISFC (relative to other participants in the training or test sub-group, as appropriate). We repeat this process twice—once using the analysis kernel (shown here as a Gaussian in the upper row of the panel), and once using a δ function kernel (lower row of the panel). **b. Projecting dynamic correlations into a lower-dimensional space.** We project the training and test data into K -dimensional spaces to create compact representations of dynamic correlations at the given order (estimated using the analysis kernel). **c. Kernel trick.** We project the dynamic correlations computed using a δ function kernel into a common K -dimensional space. These low-dimensional embeddings are fed back through the analysis pipeline in order to compute features at the next-highest order. **d. Decoding analysis.** We split the training data into two equal groups, and optimize the feature weights (i.e., dynamic correlations at each order) to maximize decoding accuracy. We then apply the trained classifier to the (held-out) test data.